

## Muon-spin-resonance study of muonium dynamics in Si and its relevance to hydrogen

S. R. Kreitzman

*TRIUMF, 4004 Wesbrook Mall, Vancouver British Columbia, Canada V6T 2A3*

B. Hitti

*Department of Physics, Rice University, Houston, Texas 77251-1892*

R. L. Lichti

*Department of Physics, Texas Tech University, Lubbock, Texas 79409-1051*

T. L. Estle

*Department of Physics, Rice University, Houston, Texas 77251-1892*

K. H. Chow

*Department of Physics, University of British Columbia, Vancouver, British Columbia, Canada V6T 1Z1*

(Received 6 December 1994)

The dynamics of transitions among muonium (Mu) states in Si have been studied by radio-frequency (rf) muon-spin-resonance techniques. A total of ten samples doped to roughly  $10^{15}$  cm $^{-3}$   $p$  type and to  $10^{16}$  cm $^{-3}$   $n$  type were investigated at temperatures from 10 to 500 K. The normalized rf asymmetry for the ionized center in the  $p$ -type samples is well described by a three-state strong-collision model involving  $\text{Mu}_{\text{BC}}^+$ ,  $\text{Mu}_{\text{BC}}^0$ , and  $\text{Mu}_T^0$ . Addition of  $\text{Mu}_T^-$  and related transitions complicates the model for intermediate  $n$ -type concentrations; however, at higher  $n$ -type levels a modified three-state model with  $\text{Mu}_T^-$  replacing  $\text{Mu}_{\text{BC}}^+$  successfully describes the charged-state intensities. Observed features are assigned to seven separate transition processes and a single set of parameters, obtained primarily from fits to two samples, provide an excellent description over the full doping range. The Mu results correlate well with the few analogous hydrogen measurements and imply rapid transitions among several hydrogen states under typical experimental conditions.

### I. INTRODUCTION

The fact that hydrogen easily enters most semiconductors and is chemically active within these materials is well established.<sup>1</sup> Hydrogen forms stable bound states with many defects and impurities; it ties up dangling bonds, passivates shallow donors or acceptors and some deep-level impurities, activates a few originally inactive impurities, and forms various complexes within extended defects. The kinetics of dopant-hydrogen passivation reactions and the structure and dynamics of the resulting complexes have been extensively studied since their discovery in the early 1980s. Much of the experimental evidence regarding diffusion of isolated hydrogen and the presence and stability of its charged states comes indirectly from hydrogen passivation and reactivation studies, or from depletion region capacitance measurements. Compared to the extensive data base on H-related complexes, direct observations of isolated H in any semiconductor are extremely sparse. Theoretical results and experiments on the muonium analog provide much of our knowledge of the states formed by atomic hydrogen as an isolated impurity in this important class of materials.

Neutral muonium [atomic notation,  $\text{Mu}=(\mu^+, e^-)$ ] is formed when an implanted positive muon captures an electron. The muonium atom is thus a very light pseudoisotope of H, with a mass only  $\frac{1}{9}$ th that of hydrogen.

Because the muon is relatively short lived with a mean lifetime of 2.2  $\mu\text{s}$ , one observes only states formed in the implantation process or during the very early stages of any reaction chain. Chemically, muonium is expected to behave essentially the same as atomic hydrogen, with strictly analogous electronic states; however, the light mass implies significant differences for physical processes such as diffusion which involve nuclear motion. For example, the larger zero-point energy of the muon implies that its energy level in a given potential well lies higher than the analogous proton state. This reduces muonium site-change barriers compared to those for hydrogen. On the other hand, energy-level positions within the semiconducting gap, which represent the ionization energies and thus depend on the reduced mass of the electron, will be essentially equal for H and Mu. The muon has a relatively large magnetic moment ( $I = \frac{1}{2}$ ,  $\gamma_\mu = 3.18\gamma_p$ ), and standard muonium research methods are generally classified as magnetic-resonance techniques. Conventional transverse-field-time-differential (TFTD) and muon-spin-rotation ( $\mu\text{SR}$ ) data demonstrate that at least three states are formed in many diamond and zinc-blende structured materials: two neutral paramagnetic states, known in the  $\mu\text{SR}$  literature as normal (Mu) and anomalous (Mu\*) muonium, and a nonparamagnetic state or states yielding the so-called diamagnetic or  $\mu^+$  signal.<sup>2,3</sup> In reality, the latter may be either an isolated  $\text{Mu}^+$  or

$\text{Mu}^-$  ion or a bound state formed with another impurity. The paramagnetic neutral Mu has an isotropic hyperfine interaction, while the  $\text{Mu}^*$  state has a small highly anisotropic hyperfine tensor axial about  $\langle 111 \rangle$  directions. Early TFTD  $\mu\text{SR}$  results show that Mu and  $\text{Mu}^*$  ionize above 230 and 120 K, respectively, in silicon, with each signal fraction recovered in the  $\mu^+$  signal at considerably higher temperatures.<sup>2</sup> The temperature offset for observation of the ionized product is due to the requirement of spin-precession phase coherence in TFTD methods. This limits observation of final states to reactions which are completed in a small fraction of the precursor muon-spin-precession period.

Over the past several years we have investigated muonium ionization reactions and site changes in silicon using longitudinal-field (LF) techniques which effectively remove the phase-coherence requirement and consequently are far more sensitive to final or intermediate states of any reaction chain. These experiments consist of two types: LF depolarization measurements using standard TD methods; and modification of the time-integral decay positron asymmetry resulting from resonant rf excitation. The LFTD experiments measure the actual loss of muon-spin polarization and are analogous to determining  $T_1^{-1}$  relaxation rates in NMR as opposed to  $T_2^{-1}$  measurements obtained from TFTD methods. Since no direct spectral information is obtained, identification of the muonium states responsible for the relaxation is indirect in LFTD measurements and requires detailed knowledge of the field dependences for each possible state. Initial LF results revealed an electron ionization-recapture charge cycle which apparently occurs in all semiconducting materials at sufficiently high temperatures.<sup>4</sup> The second technique, known as rf- $\mu\text{SR}$ ,<sup>5</sup> is analogous to standard cw-NMR methods except that resonances are detected via the decay positron asymmetry in the usual  $\mu\text{SR}$  fashion. This paper presents an essentially complete dynamic model of isolated muonium state changes in Si derived from the results of rf- $\mu\text{SR}$  experiments and consistent with the present understanding of the LF data. Preliminary results covering the  $p$ -type samples have been reported previously.<sup>6,7</sup>

Prior to the initiation of the current project a great deal of experimental and theoretical effort was expended to identify the muonium states responsible for the various  $\mu\text{SR}$  signals and to determine their electronic and structural properties. A combination of muon level-crossing resonance ( $\mu\text{LCR}$ ) data<sup>8</sup> and theoretical modeling<sup>9,10</sup> established that, of the two neutral states, the anisotropic center  $\text{Mu}^*$  is the ground state in Si and that the muon location lies near the center of a stretched Si-Si bond, i.e., in a bond-centered (BC) configuration. The unpaired electron is predominantly associated with the two nearest-neighbor Si atoms and occupies a nonbonding orbital with a node at the muon position. The isotropic neutral Mu is a rapidly diffusing state associated with the largest interstitial region in the diamond structure, i.e., the tetrahedral interstice or  $T$  site. Throughout this paper we adopt a notation which designates both the muonium charge state and site, labeling the ground state ( $\text{Mu}^*$ ) as  $\text{Mu}_{\text{BC}}^0$  and the metastable (Mu) as  $\text{Mu}_T^0$ . The

electronic equivalence of  $\text{Mu}_{\text{BC}}^0$  and  $\text{H}_{\text{BC}}^0$  has been experimentally demonstrated by comparison of the  $\mu\text{LCR}$  results with parameters from EPR data on the  $AA9$  center.<sup>11</sup> Theoretical considerations<sup>1</sup> imply that the positive ion should be stable at the BC site, i.e.,  $\text{Mu}_{\text{BC}}^+$ .  $\text{Mu}_{\text{BC}}^+$  should have a structural configuration very similar to  $\text{Mu}_{\text{BC}}^0$  since the electron is removed from the nonbonding orbital. The extended  $\text{Mu}_{\text{BC}}^0$  wave function and weak binding lead to a  $\text{BC}(+/0)$  level near the conduction-band edge, although considerably deeper in the gap than typical shallow donors. Placing a second electron in a nonbonding orbital is energetically costly, and the  $\text{BC}(0/-)$  level lies well up in the conduction band. The metastable neutral  $\text{Mu}_T^0$  has a hyperfine parameter roughly half that of the vacuum Mu atom. The ionization energy should also remain a significant fraction of the vacuum value so that the  $T(+/0)$  level should fall within the valence band. The negative ion  $\text{Mu}_T^-$  can exist, probably with a level in the upper half of the gap, since evidence for it only occurs in sufficiently highly doped  $n$ -type samples. Several theoretical results<sup>12</sup> place the  $T(0/-)$  level lower than the  $\text{BC}(+/0)$  level, leading to negative- $U$  behavior for H or Mu in Si. Very recent experiments<sup>13</sup> appear to verify negative  $U$  for hydrogen by placing the  $T(0/-)$  level near midgap. The two ionic states,  $\text{Mu}_{\text{BC}}^-$  and  $\text{Mu}_T^+$ , which are not observed because the required levels do not exist within the semiconducting gap, will not be considered further.

## II. THE DYNAMIC MODEL

The rf- $\mu\text{SR}$  results presented here provide dynamic parameters for the main transitions which occur among the four muonium states discussed above, namely  $\text{Mu}_T^0$ ,  $\text{Mu}_T^-$ ,  $\text{Mu}_{\text{BC}}^0$ , and  $\text{Mu}_{\text{BC}}^+$ . Figure 1(a) displays the basic idealized configuration-coordinate diagram involving these states, and defines the notation adopted for the various energy parameters. This notation is similar to the state labels, with subscripts carrying site information and superscripts for the charge states. For each transition the parameter labeling convention is the initial state followed by the final state in the appropriate subscript or superscript.

The solid curves in the schematic configuration-coordinate diagram of Fig. 1(a) represent states which are active in near-intrinsic and  $p$ -type samples: the two neutrals  $\text{Mu}_{\text{BC}}^0$  and  $\text{Mu}_T^0$ , and the positively charged state  $\text{Mu}_{\text{BC}}^+$ . For  $n$ -type samples the  $\text{Mu}_T^-$  state becomes important and is included in the diagram as a dashed curve. In order to discuss all samples within a single diagram we have included three particles, the implanted  $\mu^+$  and two  $e^-$ . For the  $p$ -doped materials one can think of this picture without the second electron present. There is experimental evidence that the observed charge transitions involve electrons<sup>14</sup> with the exception of a hole-capture process at low temperature in  $p$ -type samples. The configuration-coordinate diagram we present is highly idealized in at least two important aspects: first, we use essentially parabolic potential wells even far from the minima; and, second, the configuration coordinate for

transitions between different pairs of states does not, in general, follow the same path. Furthermore, since this diagram represents an operational experimental picture any kinetic energy of the muon is included at each point along the path. We take the intersections of curves for different Mu charge states to represent a barrier for combined site and charge-state changes since we cannot experimentally distinguish separate transition components. For transitions where the rf data are sensitive to the dynamics, the energy differences displayed in Fig. 1(a) are scaled to the barriers we obtain.

When considering experimentally observed dynamics

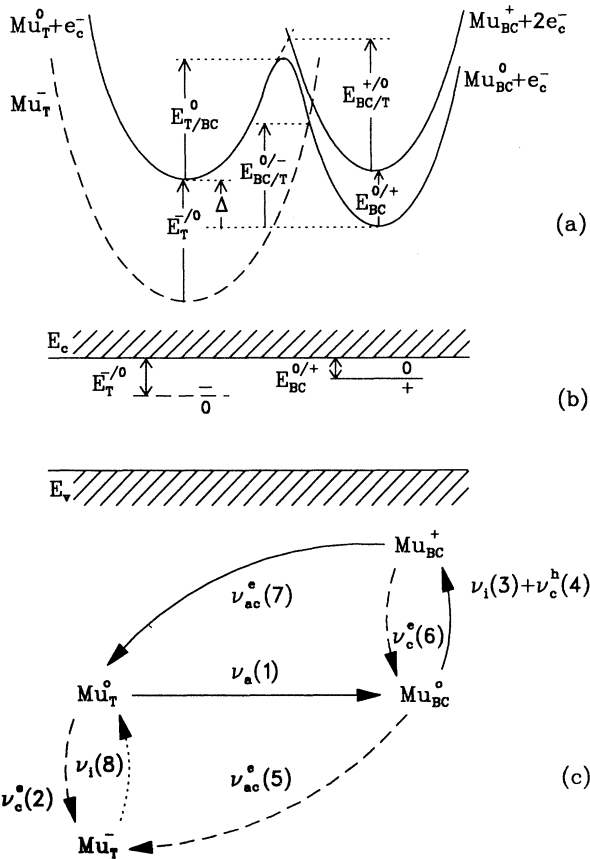


FIG. 1. (a) A schematic configuration-coordinate diagram representing the various muonium states in Si. The system includes three particles: the implanted  $\mu^+$  and two  $e^-$  ( $e^-$  is an electron at the minimum of the conduction band). The solid curves represent the states active in the *p*-type samples, and the dashed curve represents the negative charge state which is important in *n*-type samples. The barrier/ionization energy parameters obtained from the current study are:  $E_{BC}^{0/+} = 0.22$  eV,  $E_T^{0/+} = 0.39$  eV,  $E_{BC/T}^{+/-} = 0.38$  eV, and  $E_{BC/T}^{0/+} = 0.34$  eV. (b) The energy levels within the gap for muonium in Si. (c) Observed transitions among the Mu states in Si. Rate labels identify the responsible processes by number. The solid lines are for *p*-type samples and for all samples at high temperatures. The broken lines are for additional transitions in *n*-type samples at low temperatures. The dotted line represents the possible thermal loss of an electron by  $Mu_T^-$ .

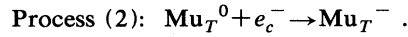
within this system it must be stressed that one is usually operating far from equilibrium in terms of relative populations of the muonium states. The two sites are initially populated in some ratio determined primarily by the kinetics of the  $\mu^+$  implantation process, while the initial charge-state mix at each site is governed by the concentrations of electrons and holes liberated during thermalization. Currently, very little is known about the details of these muon-stopping processes. Except at the highest temperatures, the muon lifetime limits dynamic observations to the initial stages of the reaction chain leading toward equilibrium in the muonium state occupation probabilities. The eventual steady-state mix of populations can more easily be considered using the energetics displayed in Fig. 1(b), showing the electronic levels residing within the gap for muonium in Si. Since there are seldom more than one or two muons present in the sample at a given time, the presence of the muonium states can be completely ignored in determining electron ( $n_e$ ) and hole ( $n_h$ ) concentrations, or equivalently the location of the Fermi level. These are calculated using known parameters for the band gap and dopant energy levels in Si, and measured dopant concentrations for each sample. At room temperature in near-intrinsic and *p*-type samples the Fermi level is at or below midgap, most likely below either muonium-related level implying that  $Mu_T^0$  and  $Mu_{BC}^+$  are the expected states for the respective sites. Since  $Mu_T^0$  is the metastable neutral, after a sufficiently long time the positive charge state should be dominant in *p*-type materials. In contrast, for strongly *n*-type materials at room temperature, the Fermi level lies above both muonium levels leading to  $Mu_T^-$  and  $Mu_{BC}^0$  at the two sites. In this case, since  $Mu_{BC}^0$  is the neutral ground state, conversion to the charged state may be much less likely even though the excess electron concentration increases the electron-capture rate by the neutral state and hence pushes the system toward eventual  $Mu_T^-$  occupancy. Since the muonium system is quite far from equilibrium over most of the data range, we have not explicitly built in the eventual equilibrium state occupations other than to use the correct equilibrium carrier concentrations; i.e., detailed balance arguments were not used to place constraints on relative rates for various processes. Because our observations imply that most charge-state changes involve electrons, we have chosen to use an energy scheme appropriate to electron processes in Fig. 1(a). Low-temperature TFTD- $\mu$ SR signal intensity ratios indicate that the initial populations in the BC and T sites are approximately equal.<sup>2</sup> Also, for near-intrinsic samples about 5% of the states are charged. As an example of the nonequilibrium conditions, this means that, in intrinsic and *p*-type cases, the system is started with an  $e^-$  nearly always occupying the BC(+ / 0) energy level even though  $Mu_{BC}^+$  is the expected final state at that site as dictated by the Fermi-level position. The positions of the Fermi level will also influence which transitions dominate in each sample. Possible temperature dependences in the dynamic parameters have been ignored in our model.

We discuss anticipated transition processes by considering possible paths out of each of the four states. Processes which involve direct transitions between the posi-

tive and negative charge states are second order in capture cross sections and will be ignored as considerably less likely than competing routes. Likewise, paths with obviously higher barriers can also be ignored as having low probability. We have also left out a few of the possible hole capture processes because our experiments imply that electron processes dominate them. These arguments leave the following set of likely transition paths which must be considered. Starting with the neutral states, expected transitions out of the metastable  $T$  site include the site change to the stable configuration.

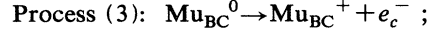


and, in  $n$ -type samples, capture of a conduction electron to form the negative ion,

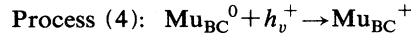


A third possible path, a direct transition from  $\text{Mu}_T^0$  to the ionized  $\text{Mu}_{\text{BC}}^+$  state, is much less likely than process (1), which is available in all samples, since this alternative involves either hole capture or excitation of the muonium electron to the conduction band in addition to the site change. The barrier is larger than for process (1) even without a prefactor reduction related to the charge-state change, implying a lower probability for this route. It is ignored in our model.

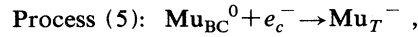
For the stable bond-centered neutral there are three likely exit processes: simple thermal ionization,



and the two carrier capture processes



and



which are active only in appropriately  $p$ - or  $n$ -doped samples, relatively. In addition to  $e^-$  capture, process (5) involves a site change implying a barrier. This is one of the combined site and charge-state changes which we label as activated capture and treat as a single step since we cannot resolve the actual reaction path. An additional possible path into the (metastable)  $T$  site as a neutral, i.e.,  $\text{Mu}_{\text{BC}}^0 \rightarrow \text{Mu}_T^0$ , appears always to be unfavorable since the barrier will be  $E_{\text{BC}/T}^0 = E_{T/\text{BC}}^0 + \Delta$ , and the expected value for  $\Delta$  is at least a few tenths of an eV.<sup>15</sup>

For the charged states there appear to be fewer favorable options. For the positive charge state the two likely processes both involve electron capture:

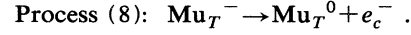


and



Assuming the BC(+/0) level is in the upper part of the gap as expected, thermal excitation of a hole into the valence band is highly unlikely and can be ignored. Note that process (7) represents a second activated capture

process since it involves a  $\text{BC} \rightarrow T$  site change. For the negative ion only thermal ionization appears to be likely,



Because  $\text{Mu}_{\text{BC}}^0$  is more stable than  $\text{Mu}_T^0$ , direct conversion to  $\text{Mu}_{\text{BC}}^0$  via a combined site and charge-state change might be possible. The energetics in Fig. 1(a) imply a larger barrier for this option than for process (8); thus it has not been included. The remaining alternatives involve hole capture and would only be active under conditions where the negative charge state is not expected to occur (i.e., in  $p$ -type samples), although such processes may serve to quickly neutralize any  $\text{Mu}^-$  ions formed during implantation in  $p$ -type samples.

Figure 1(c) shows transition paths among the four muonium states represented by the above processes. As will be demonstrated, we have identified features in the rf data associated with each process, and have extracted dynamic parameters for the first seven. The exception is process (8) (dotted line), where  $\text{Mu}_T^-$  is stable to high temperatures in  $n$ -type materials. The paths shown with solid lines in the figure represent those active at high temperatures in all samples, and the only paths important in  $p$ -type samples. The paths shown with broken lines are the additional interactions present in  $n$ -type materials and will be shown to dominate the Mu dynamics in  $n$ -type samples below room temperature.

Some information on muonium dynamics exists from other types of measurements. Older TTFD- $\mu$ SR results<sup>2</sup> yielded an ionization energy of  $E_{\text{BC}}^{0/+} = 0.17$  eV for  $\text{Mu}_{\text{BC}}^0$ , extracted from the increase in the  $\text{Mu}^*$  relaxation rates above 120 K, but simulations of the recovery in the  $\mu^+$  signal suggest a somewhat higher value of about 0.25 eV. Similar attempts to obtain an ionization energy for metastable  $\text{Mu}_T^0$  resulted in a much wider set of values ranging from 0.11 to 0.39 eV, and displayed considerable sample dependence.<sup>2</sup> Decay positron channeling experiments on near-intrinsic samples determined that between about 270 and 400 K the muon is almost exclusively at or near the BC site.<sup>16</sup> Over the same range  $\mu$ SR data identify only an ionized muonium signal, implying that the dominant state is  $\text{Mu}_{\text{BC}}^+$ . Fits of the LF relaxation data show that the neutral state involved in the high-temperature charge cycle has a hyperfine parameter close to that for  $\text{Mu}_T^0$  rather than that for the low-temperature stable state  $\text{Mu}_{\text{BC}}^0$ .<sup>4</sup> The longitudinal data were fit with a simplified two-state model with a  $\text{Mu}^{0/+}$  state assumption, and yielded an ionization energy of 0.34 eV. The current rf- $\mu$ SR results are sensitive to the charge-cycle onset region, but no information is available in the temperature range where the majority of the LF data were obtained. The sensitivity of the present data to the beginning of charge exchange is utilized to obtain BC to  $T$  site-change parameters.

### III. EXPERIMENTAL METHODS

The arrangement of  $\mu$ SR counters used was a standard geometry for longitudinal-field experiments in which the static magnetic-field direction, counter axis, and initial spin direction are collinear along the  $z$  axis as shown in

Fig. 2. All of the data presented in this work have been taken in the time-integral mode, where one measures the steady-state integrated count rate in the forward ( $F$ ) and backward ( $B$ ) positron counters with the radio frequency on (+) and off (−). Such a state is given by<sup>17</sup>

$$\begin{aligned} N_{F/B}^{\pm} &= N_{F/B}^0 \int_{-\infty}^t \nu_{\mu} e^{-\nu_{\mu}(t-\tau)} [1 + A_{F/B} G_{zz}^{\pm}(t-\tau)] d\tau \\ &= N_{F/B}^0 \int_0^{\infty} \nu_{\mu} e^{-\nu_{\mu}t} [1 + A_{F/B} G_{zz}^{\pm}(t)] dt, \end{aligned} \quad (3.1)$$

where  $N_{F/B}^0$  is the initial positron flux reflecting the beam intensity and the geometry of the counters,  $\nu_{\mu}$  is the inverse of the muon lifetime,  $A_{F/B}$  is the asymmetry parameter associated with a given counter/sample geometry arising from asymmetrical preference of the positron to decay in the direction of the muon polarization, and  $G_{zz}^{\pm}(t)$  is the  $z$  component of this polarization when the applied static magnetic field is also in the  $z$  direction. The important physics is located in the term containing the time-dependent muon polarization. The function  $G_{zz}^{\pm}(t)$  depends on the populations and spin dynamics for each muonium center, as well as the dynamics of transitions between muonium states and any other interactions which may affect the time history of the muon spin polarization. For this application we have used a limited set of muonium transitions which allows an analytical solution using Laplace transform methods. If  $G_{zz}^{\pm}(s)$  is the Laplace transform of  $G_{zz}^{\pm}(t)$ , then, using the above expression, the theoretical task is to evaluate this function at a characteristic rate equal to the inverse muon lifetime  $G_{zz}^{\pm}(s)|_{s=\nu_{\mu}}$ . Section V and the Appendixes outline the spin dynamical calculations which are required to make this evaluation within our working model.

A feature of the integral rf- $\mu$ SR experiment which is of great utility for the present measurements is that the

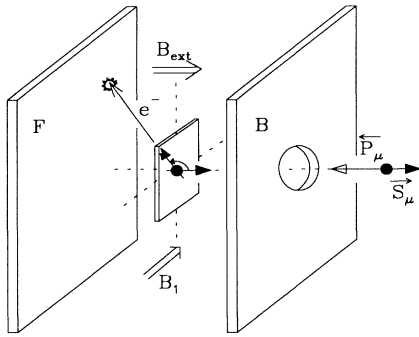


FIG. 2. Longitudinal field geometry for an integral rf- $\mu$ SR experiment. The effective magnetic field on the muons comes from the applied field  $B_{\text{ext}}$  and the rf field  $B_1$ . Off resonance the effective field in the rotating frame is parallel to the spin, and the muons do not precess. On-resonance the effective field is equal to the rf field  $B_1$  and the muon spins precess in this field until they decay into positrons. The decay positrons are emitted preferentially along the spin direction of the muon, therefore allowing the muon polarization to be measured.

presence of a strong rf field implies a specific form of  $G_{zz}^{\pm}(t)$  when a resonance condition is satisfied for one of the muonium centers. To accurately determine the degree to which this resonance condition is satisfied under experimental conditions requires that the integral counts be combined in the following manner:

$$A_{\text{rf}} = \frac{N_F^+ - N_F^-}{N_F^+ + N_F^-} - \frac{N_B^+ - N_B^-}{N_B^+ + N_B^-}, \quad (3.2)$$

which is called the rf asymmetry and serves to isolate the integrated change in the LF time-dependent asymmetry due to the rf irradiation. For a system with several potential rf resonances Sec. V describes a generalization of the above expression for the rf asymmetry.

The design of the rf coil which produces the oscillating transverse magnetic field driving the resonance is certainly the most innovative feature of our system. Fundamentally it is a nonresonant broadband 50- $\Omega$  delay line. The idea of using such a delay line for magnetic resonance was investigated by Low and co-workers<sup>18,19</sup> and that work inspired our development effort. Basically, the coil consists of a number of turns of a flat conductor wrapped around two anodized Al rods that themselves are securely fixed to a grounded mounting framework. The geometry, ideal for solid-state  $\mu$ SR applications, is similar to the flat coil of Ref. 19, but uses a flat conductor wrapped on insulated (i.e., anodized) cylindrical posts rather than a round insulated conductor pressed onto a flat ground plane to create the distributed capacitance and inductance. The broadband characteristic of the coil can easily be adjusted to exhibit a standing-wave ratio (SWR) of less than 1:1.5 over the entire 10–250-MHz band of our system. This has proven to be very suitable for swept-frequency experiments. With an input power of 250 W the coil yields a rotating rf field component  $B_1 \approx 7$  G. The rf coupling scheme used in the experiment, unlike the usual case in NMR, is totally nonresonant. The rf current runs from the amplifier, down the transmission coaxial line, through the windings of the delay-line coil to create the magnetic field, and finally through the return leg into a high power oil-mediated 50- $\Omega$  load. Details of the coil assembly and rf coupling scheme will be published elsewhere.

Using rf resonant techniques at a cw meson facility like TRIUMF entails further difficulties due to the rather high rf heating effects arising from the surface resistance of the coil and capacitor rods.<sup>5</sup> Thus even though the coil is nominally a 50- $\Omega$  delay line, this effect results in a relatively large source of heat in the direct vicinity of the sample. To minimize the systematic errors in the temperature measurement from these effects, or from eddy currents within the sample, the following method was adopted. A set of test samples was mounted on a boron nitride substrate that protruded out of the coil so that a Au-Fe(0.07%) thermocouple could be inserted into the substrate. This thermocouple was used to measure the temperature gradient between the substrate and a calibrated Si diode located on the Cu housing that holds the coil assembly. Calibration tests show that the temperature of the substrate reflects the temperature within the rf

coil to within  $\pm 0.5$  K, except for very low-resistivity samples where eddy current heating of the sample itself is strong. These test samples were then measured over the range of power and frequency conditions used in all experiments reported here. The temperature difference between the diode and the test samples had a simple dependence on temperature and applied power. These corrections were applied to all of the data with the exception that when the thermocouple was in place during the actual run, the temperature correction was made directly rather than using this calibration technique.

Since the rf was periodically modulated on and off for normalization, in order to further stabilize the temperature the rf duty cycle was always kept constant at 50%, and the rf-on time, usually about 2 s, was not allowed to vary by more than 20%. In this way the thermal conditions in the rf cell were maintained in a steady state, independent of external conditions of the experiment. To accomplish this the control software provides for a monitor on the incoming muon flux. When this monitor varies outside preset limits (20% in this case) the software automatically deactivates the data acquisition while at the same time switching into a mode that maintains the rf conditions as they would be during data acquisition. Thus any significant fluctuation in the beam puts the experiment into this inactive mode which is thermally identical to the running conditions. When nominal operating conditions return, the software switches back to the active acquisition state with the assurance that thermal conditions have not varied significantly during the standby period. During such excursions, the temperature control (driven from the thermometers located on the mounting arms) remains engaged and the internal steady state maintained by this arrangement implies that the temperature gradients do not significantly change.

To ensure the reproducibility of our data, steps were also taken to stabilize the rf power against voltage fluctuations in the mains which directly affects the plate voltage of the final stage. To this end the rf amplifier is fitted with a sophisticated feedback system controlled by the rectified output of a detector diode which is driven by the sampling port of a precision broadband directional coupler. Other elements of our setup consist of a pickup

coil, power monitors, and fast-acting protective trip circuits. This last item is particularly relevant since without such protection a failure can easily result in a very large standing-wave ratio, often to the detriment of expensive samples, cryostats, flanges, thermometers, and other components in the vicinity of a high voltage or current node. The implementation of this protective circuit relies on a fast rf switch that will very quickly (submicrosecond) shut off the input signal to the amplifier whenever significant reflected power is detected. Since this will occur whenever any element of our system ceases to be  $50 \Omega$ , this protection is globally sensitive to rf faults.

#### IV. SAMPLES

Three Si samples doped with boron, one with gallium, one with indium, and five with phosphorus in the concentration range  $10^{11}$ – $10^{16}$   $\text{cm}^{-3}$  were studied. The concentration of dopants as obtained from photoluminescence measurements is summarized in Table I. The diameters vary between 15 and 20 mm and most samples are 1–2 mm thick. All samples were obtained from various commercial sources. They were grown using the float-zone technique and doped during the growth process. Sample orientations are also listed in Table I, and indicate the crystal axis parallel to the applied field and initial muon spin-polarization direction. The temperature dependence of several observed features vary with this sample orientation. *P11*, *P13*, *N12*, and *N13* were studied previously in transverse field by the university of Zürich group.<sup>2</sup> Longitudinal-field measurements are available on *N14*,<sup>20</sup> and on some of the other *n*-type samples (unpublished data).

#### V. DATA ANALYSIS

As in conventional magnetic resonance, it is convenient to treat the effect of the rf field on a spin system by transformation into a frame rotating at the rf oscillator frequency  $\omega$  around  $\hat{z}$ , the direction of the static magnetic field  $\mathbf{B}_{\text{ext}}$ . For the general case the effective field  $\mathbf{B}_{\text{eff}}$  in the rotating reference frame (RRF) is composed of a modified  $\hat{z}$  component and an rf field  $\mathbf{B}_1$  in the  $(\hat{x}_R, \hat{y}_R)$

TABLE I. Summary of the sample orientations and the P, B, Al, Ga, In, and net carrier (*C*) concentrations. The ionization energies for P, B, Al, Ga, and In in Si are 45.5, 44.5, 68.5, 72, and 160 meV, respectively.

Sample	Axis	$C_P$ ( $\text{cm}^{-3}$ )	$C_B$ ( $\text{cm}^{-3}$ )	$C_{\text{others}}$ ( $\text{cm}^{-3}$ )	Type	$C_C$ ( $\text{cm}^{-3}$ )
<i>P11</i>	110	$1.4 \times 10^{12}$	$1.1 \times 10^{12}$	Al $0.6 \times 10^{12}$	<i>p</i>	$3.0 \times 10^{11}$
<i>P13</i>	110	$0.5 \times 10^{13}$	$1.5 \times 10^{13}$		<i>p</i>	$1.0 \times 10^{13}$
<i>P14</i>	100	$0.3 \times 10^{14}$	$4.4 \times 10^{14}$		<i>p</i>	$4.1 \times 10^{14}$
<i>P15</i>	111			Ga $1.2 \times 10^{15}$	<i>p</i>	$1.2 \times 10^{15}$
SiIn	111			In $2.0 \times 10^{15}$	<i>p</i>	$2.0 \times 10^{15}$
<i>N12</i>	111	$2.6 \times 10^{12}$	$0.2 \times 10^{12}$		<i>n</i>	$2.4 \times 10^{12}$
<i>N13</i>	111	$3.4 \times 10^{13}$	$1.5 \times 10^{13}$		<i>n</i>	$1.9 \times 10^{13}$
<i>N14</i>	111	$4.9 \times 10^{14}$	$2.4 \times 10^{12}$		<i>n</i>	$4.9 \times 10^{14}$
<i>N15</i>	100	$1.5 \times 10^{15}$			<i>n</i>	$1.5 \times 10^{15}$
<i>N16</i>	111	$5.0 \times 10^{15}$			<i>n</i>	$5.0 \times 10^{15}$

plane, where  $(\hat{x}_R, \hat{y}_R, \hat{z})$  are the unit vectors in the RRF. The effective field is then  $\mathbf{B}_{\text{eff}} = [(\omega_0 - \omega)/\gamma] \hat{z} + B_1 \hat{\rho}(\phi)$ , where  $\omega_0 = \gamma B_{\text{ext}}$  is the Larmor frequency in  $\mathbf{B}_{\text{ext}}$ ,  $\gamma$  the muon gyromagnetic ratio, and  $\hat{\rho}(\phi) = \hat{x}_R \cos\phi + \hat{y}_R \sin\phi$ . With  $\mathbf{B}_{\text{eff}}$  directed along a unit vector  $\hat{r}$  ( $\hat{r} = \hat{z} \cos\theta + \hat{\rho} \sin\theta$ ), and assuming unit initial polarization parallel to  $\hat{z}$ , the time evolution of the  $\hat{z}$  component of the polarization in the absence of relaxation is given by

$$P_z^+(t) = \cos^2\theta + \sin^2\theta \cos\omega_{\text{eff}} t, \quad (5.1)$$

where  $\omega_{\text{eff}} = \sqrt{(\omega_0 - \omega)^2 + \omega_1^2}$  is the precession frequency in the effective field,  $\omega_1 = \gamma B_1$  is the precession frequency in the rf field, and  $\cot\theta = (\omega_0 - \omega)/\omega_1$ .

Experimentally, the rf field acts on all muons stopped in the sample. On resonance, the frequency  $\omega$  is matched to an energy-level splitting ( $\varepsilon_i - \varepsilon_j$ ) for one of the muonium centers. For the ionized states  $\text{Mu}^\pm$  these are just the Zeeman states of the muon spin, while in the neutral centers the splitting is a function of both the applied magnetic field and the hyperfine interaction. Energy is transferred between the rf field and the on-resonance muonium states, inducing transitions between the active eigenstates  $|i\rangle$  and  $|j\rangle$ . These transitions are observed as a change in the LF polarization, detected as in Eq. (3.2). The sum of counts in the  $F(B)$  counter under rf excitation is given by Eq. (3.1), with  $G_{zz}^+(t)$  modified by the rf to give the following time-integral equation:

$$N_{F/B}^+ = N_{F/B}^0 \int_0^\infty \nu_\mu e^{-\nu_\mu t} \{1 \mp A \pm A_{\text{rf}}^{ij} [1 - P_z^{ij,+}(t)]\} dt, \quad (5.2)$$

where the indices  $\{i, j\}$  have been introduced to generalize the rf response between any two eigenstates  $|i\rangle$  and  $|j\rangle$ ,  $A$  is the decay asymmetry in the absence of the rf field, and  $A_{\text{rf}}^{ij}$  is the active asymmetry associated with the resonant muonium state. In rf- $\mu$ SR experiments the quantity measured is  $A_{\text{rf}}^{ij}$ . An equation similar to Eq. (5.2) but with  $P_z^{ij,+}(t)$  replaced by  $P_z^{ij,-}(t)$  defines the integral counts in the absence of a rf field ( $N_{F/B}^-$ ). By substituting  $N_{F/B}^+$  from Eq. (5.2) [ $P_z^{ij,+}(t)$  from Eq. (5.1)] and the equivalent quantity  $N_{F/B}^- [P_z^{ij,-}(t) = 1]$  into Eq. (3.2) and noting that the sum of counts with the rf on and off in the forward and backward counters approximately equals  $2N_{F/B}^0$  and  $2N_{B/B}^0$ , respectively, it can be shown that  $A$ ,  $N_{F/B}^0$ , and  $N_{B/B}^0$  drop out and one obtains a Lorentzian line shape for the rf-induced asymmetry

$$A_{\text{rf}} = \sum_{ij} A_{\text{rf}}^{ij} \frac{\omega_1^{ij2}}{\nu_\mu^2 + (\omega_0^{ij} - \omega)^2 + \omega_1^{ij2}}. \quad (5.3)$$

The summation is over all possible transitions, for each line (transition  $ij$ ) the on-resonance amplitude [ $\omega_0^{ij} = \omega$  in Eq. (5.3)] is equal to  $A_{\text{rf}}^{ij}(0) = A_{\text{rf}}^{ij} \omega_1^{ij2} / (\nu_\mu^2 + \omega_1^{ij2})$ , and the half-width at half maximum is equal to  $\delta\omega^{ij} = \sqrt{\nu_\mu^2 + \omega_1^{ij2}}$ . Then Eq. (5.3) can be written in a more standard form,

$$A_{\text{rf}} = \sum_{ij} A_{\text{rf}}^{ij}(0) \frac{\delta\omega^{ij2}}{(\omega_0^{ij} - \omega)^2 + \delta\omega^{ij2}}. \quad (5.4)$$

The normal operational mode for these rf- $\mu$ SR experi-

ments is to use a fixed rf frequency and to sweep the external field through the region of the desired resonance. This is the mode we used to detect the lines associated with the ionized  $\text{Mu}^\pm$  and the  $\text{Mu}_T^0$  states. However, energy levels for  $\text{Mu}_{\text{BC}}^0$  have very weak field dependences in the low-field region relevant to our studies. Thus it was necessary to use a swept-frequency, fixed-field method to detect resonances from this center. Typical rf- $\mu$ SR data are depicted in Figs. 3, 4, and 5 for  $\text{Mu}^\pm$ ,  $\text{Mu}_T^0$ , and  $\text{Mu}_{\text{BC}}^0$ , respectively. The amplitude as a function of field or frequency is generated by combining the integral counts in the forward and backward positron counters as given in Eq. (3.2). The signals are fitted to Eq. (5.4) to yield the on-resonance amplitude, width, and resonant frequency for each line. Additional analysis is then necessary to extract the temperature dependence of the normalized asymmetry for each muonium center.

The diamagnetic amplitude in Fig. 3 is measured in the P11 sample at 310 K, with the oscillator frequency fixed at 27.1 MHz and the applied field scanned around 2 kG. An input rf power level of 250 W produces a  $B_1$  of about 7 G inside the coil. At this rf field  $\omega_1$  is of the order of  $\nu_\mu$ , so the on-resonance amplitude  $A_{\text{rf}}(0)$  depends on the rf power. Therefore, for every separate experimental set up (rf power, sample position, collimation, detector geometry, etc.) a calibration run was performed on a  $\text{CaCO}_3$  sample at room temperature to normalize the on-resonance amplitude. The normalized  $\text{Mu}^\pm$  asymmetry in Si is then given by  $0.80 A_{\text{rf}}^{\text{Si}}(0) / A_{\text{rf}}^{\text{CaCO}_3}(0)$ , where 0.80 was obtained by comparing the  $\text{CaCO}_3$  asymmetry in a weak TF to that of Al which is known to give the full experimental asymmetry. The filled circles in Figs. 6 and 7 show the normalized rf asymmetry for  $\text{Mu}^\pm$  as a function of temperature for the eight samples studied in detail. As long as  $\delta\omega$  is due only to lifetime and power broadening, the normalized asymmetry will accurately represent the fractional occupation of the diamagnetic state. For  $p$ -type samples this is the case for all of the  $\text{Mu}^\pm$  data up to the temperature at which the diamagnetic amplitude starts to drop. As discussed below this drop is due to an

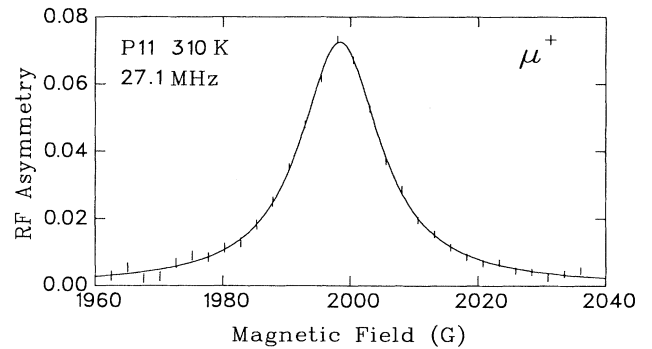


FIG. 3. Example of the  $\text{Mu}^\pm$  signal used to measure the diamagnetic amplitude as a function of temperature in Si. This particular resonance was detected in the P11 sample at 310 K, with the oscillator frequency fixed at 27.1 MHz and a  $B_1$  of about 7 G, by varying the applied field from 1960 to 2040 G by steps of 2.5 G.

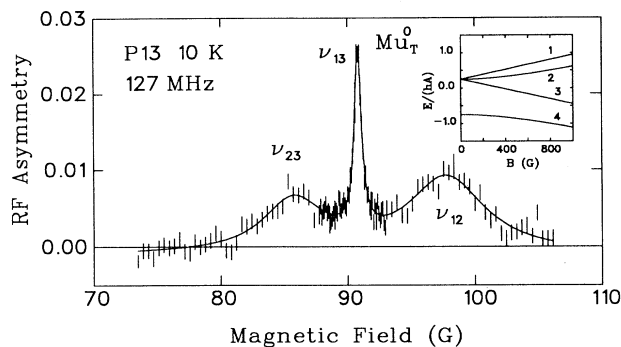


FIG. 4. The intratriplet  $\text{Mu}_T^0$  signal as measured in the *P13* sample at 10 K by a field scan around 90 G at a fixed frequency of 127 MHz and a  $B_1$  of about 3 G. The three peaks are the  $|2\rangle \leftrightarrow |3\rangle$ ,  $|1\rangle \leftrightarrow |3\rangle$ , and  $|1\rangle \leftrightarrow |2\rangle$  transitions. Displayed in the inset is the Breit-Rabi diagram that represent the hyperfine energy levels for isotropic muonium in Si as a function of the magnetic field. The hyperfine frequency of Mu in Si ( $A$ ) is 2006.3 MHz.

additional relaxation process associated with charge exchange, which introduces an extra broadening mechanism.

Figure 4 shows the intratriplet  $\text{Mu}_T^0$  signal in the *P13* sample at 10 K, as detected using a field scan around 90 G with a fixed frequency of 127 MHz. The field dependence of the energy levels, i.e., the Breit-Rabi diagram, for this system,<sup>2</sup> displayed in the inset, consists of a triplet with an unequal field-dependent splitting and a singlet separated in zero field from the triplet by the hyperfine interval. The narrow central line results from the two-photon transition  $|1\rangle \leftrightarrow |3\rangle$ . Since the properties of the double quantum line are not needed to clarify the dynam-

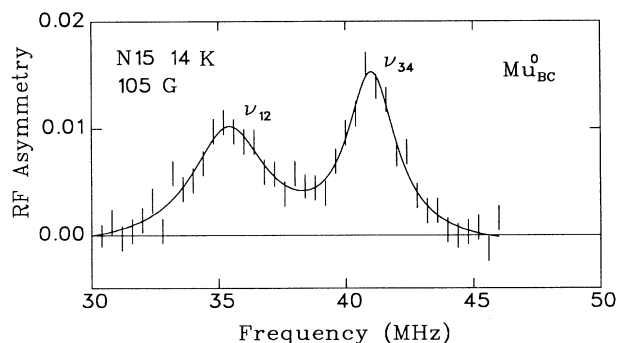


FIG. 5. A typical  $\text{Mu}_{BC}^0$  resonance measured by a frequency scan around 40 MHz with a fixed field of 105 G and a  $B_1$  of approximately 2 G. This resonance is from *N15* and was taken at 14 K. It is necessary to use a swept-frequency fixed-field mode to detect the  $\text{Mu}_{BC}^0$  resonance because the energy levels have a weak field dependence in the relevant region.

ical model, we will not discuss it further in this paper, although a description of it is found in Ref. 5. The lower and upper lines correspond to the single-photon transitions  $|2\rangle \leftrightarrow |3\rangle$  and  $|1\rangle \leftrightarrow |2\rangle$ , respectively. For these measurements the rf power is set to  $\approx 50$  W, which corresponds to a  $B_1$  of about 3 G. In this situation  $\omega_1 \gg 2\pi\nu_\mu$ , and thus the signal is power broadened and saturated so that the amplitude directly reflects the state occupation. In a low external field ( $\approx 90$  G) the singlet in the Breit-Rabi diagram is isolated from the triplet by a very large splitting, therefore the single-photon transitions  $|1\rangle \leftrightarrow |4\rangle$  and  $|3\rangle \leftrightarrow |4\rangle$  are at frequencies too high to be experimentally observable. Furthermore half the asymmetry is lost at low field because of the high-frequency oscillation of the longitudinal polarization in the mixed spin state. Taking into account this lost polarization and the unobserved lines the  $\text{Mu}_T^0$  fractions shown in Fig. 6 for the *P13* and *P14* samples by the dashed lines are given by  $(4/A)[A_{\text{H}}^{12}(0) + A_{\text{H}}^{23}(0)]$ . The  $\text{Mu}_T^0$  signals in *N13* and *N15* were too broad to measure with rf, and no searches were made in the remaining samples. In the *N13* sample we have observed the  $\text{Mu}_T^0$  signal at higher frequencies with a new microwave spectrometer.<sup>21</sup>

The  $\text{Mu}_{BC}^0$  signal in Fig. 5 is measured in the *N15* sample at 14 K and a fixed field of 105 G by scanning the

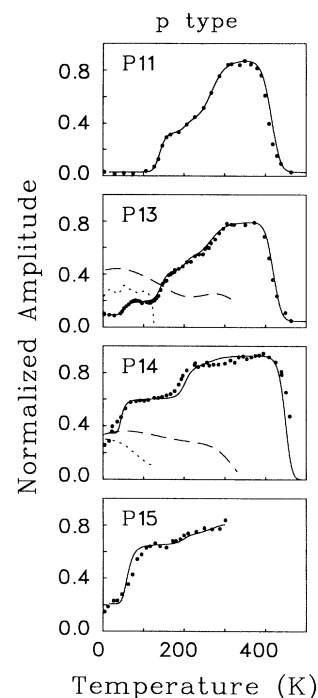


FIG. 6. Normalized rf amplitude for diamagnetic muonium (filled circles),  $\text{Mu}_T^0$  (dashed line) and  $\text{Mu}_{BC}^0$  (dotted line). The muonium amplitudes in *P11* and *P15* were not measured. The solid line for *P11* is the result of fitting to Eq. (6.1), while those for the other samples were obtained by keeping the parameters from *P11* fixed and varying only the crystal axis and dopant concentration and fitting the initial amplitudes.

frequency around 40 MHz. The hyperfine energy-level diagram for anisotropic  $\text{Mu}_{\text{BC}}^0$  depends on the angle between the  $\langle 111 \rangle$  symmetry axis and the applied magnetic field. With the magnetic field directed along the  $[100]$  axis the four possible  $\langle 111 \rangle$  symmetry axes are equivalent and at an angle of  $54.7^\circ$  with respect to the field. Under these conditions the two lines at 35.7 and 41.2 MHz are the  $|1\rangle \leftrightarrow |2\rangle$  and  $|3\rangle \leftrightarrow |4\rangle$  transitions. To estimate the fraction of the  $\text{Mu}_{\text{BC}}^0$  state in each sample one has to account for the sample orientation, the lines that are not observed, the asymmetry lost in the partially mixed spin state, and the fact that these signals were not always saturated. Due to the difficulty of correcting for the unsaturated signals the absolute values of the  $\text{Mu}_{\text{BC}}^0$  fraction shown in Fig. 6 for the  $P13$  and  $P14$  samples and Fig. 7 for the  $N12$ ,  $N13$ , and  $N15$  samples by the dotted lines are rather uncertain. However, these effects do not change their temperature dependences since the relative values are accurately determined. The  $\text{Mu}_{\text{BC}}^0$  signals in  $P11$ ,  $P15$ , and  $N14$  were not measured.

Since  $\text{Mu}_T^-$  and  $\text{Mu}_{\text{BC}}^+$  are diamagnetic, they give rf- $\mu\text{SR}$  and ordinary  $\mu\text{SR}$  spectra similar to that of  $\mu^+$ . As a consequence, these two states cannot be dis-

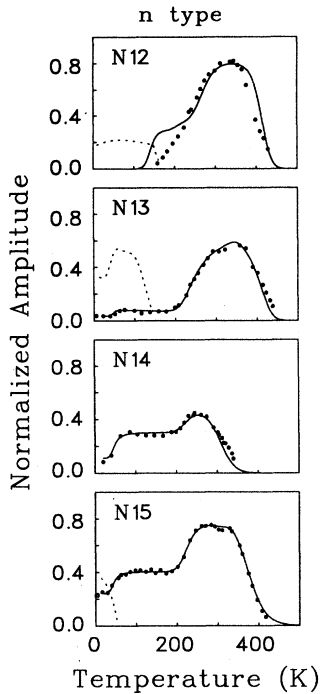


FIG. 7. Normalized rf amplitude for diamagnetic muonium (filled circles) and  $\text{Mu}_{\text{BC}}^0$  (dotted line). The  $\text{Mu}_T^0$  signal for  $N13$  and  $N15$  was too broad to measure with rf- $\mu\text{SR}$ , but in the case of the  $N13$  sample it was observed with microwave spectrometer (Ref. 21). No other muonium amplitudes were measured. The solid line for  $N15$  is the result of fitting to Eq. (6.1), while those for the other samples were obtained by keeping the parameters from  $P11$  or  $N15$  fixed and varying only the crystal axis and dopant concentration and fitting the initial amplitudes.

tinguished spectroscopically. Instead we have used the dynamic information obtained in this experiment along with theoretical expectations to infer the relative contributions of these two charged centers to the diamagnetic amplitude.

## VI. RESULTS AND DISCUSSION

The rf-induced asymmetry, which is the directly measured quantity experimentally, can be obtained quite generally by substituting Eq. (5.2) and the equivalent equation for  $N_{\bar{F}/B}$  into Eq. (3.2) yielding

$$A_{\text{rf}} = \sum_{ij} A_{\text{rf}}^{ij} [\nu_{\mu} \bar{P}_z^{ij,-}(\nu_{\mu}) - \nu_{\mu} \bar{P}_z^{ij,+}(\nu_{\mu})], \quad (6.1)$$

where  $\bar{P}_z^{ij,-}(\nu_{\mu})$  and  $\bar{P}_z^{ij,+}(\nu_{\mu})$  are the Laplace transforms of the polarization with the rf off and on, respectively. Under typical experimental conditions only one set of spin states  $i, j$  from a single Mu center contribute to this expression; however, the Laplace transforms associated with that particular spectral line contain the full polarization history for all precursor states and transition paths. A three-state strong collision model with ionization and capture rates to describe the dynamics between the various muonium centers in Si, as outlined in Sec. II, is used to write integral rate equations that describe the time evolution of polarization for each center (see Appendix A). The specific muonium states which are included are the two neutrals and a single charged state. This treatment yields an analytical solution when the important transitions are included. Only in a few samples, over a narrow temperature range, are all four states relevant; for these samples a four-state model will be more appropriate. However, since the two ionized states display identical spin dynamics and only one of them is active in nearly all circumstances, the three-state model does a satisfactory job of describing the behavior. All of the dynamic parameters quoted in this paper were obtained from a fit to the rf-induced asymmetry for the diamagnetic signal. Therefore, the rate equations were solved using Laplace transform methods for the case where the diamagnetic signal is on-resonance [ $P_z^+(t) = \cos \omega_1 t$ ; Eq. (5.1)]. The rf data for  $\text{Mu}_{\text{BC}}^0$  and  $\text{Mu}_T^0$  along with longitudinal relaxation measurements for several samples were only used as qualitative checks of overall consistency in assignments of states and transition processes.

The Laplace transform of the diamagnetic polarization is a function of the initial population of each state, the transition rates for the processes included in the model introduced in Sec. II, the strength of the rf field  $B_1$ , the dephasing of the polarization in the precursor  $\text{Mu}_{\text{BC}}^0$  state due to the anisotropic hyperfine interaction, and the depolarization at high temperature due to the charge-state cycle that involves  $\text{Mu}_T^0$ . Other possible depolarization mechanisms are not accounted for in the present model, but may affect the experimental results if the associated rate is comparable to or faster than transitions out of the depolarizing state. Such mechanisms are in fact present for some of the  $n$ -type samples where the three-state model is already poor, and are discussed qualitative-

ly when dealing with those samples. The simplest temperature-dependent rate expressions consistent with our understanding of each transition process were used. The  $e^-$  and  $h^+$  capture processes at a single site were fit using rates of the form  $v_c = nv\sigma$  using the appropriate free-carrier density, the mean thermal velocity for the carriers, and the cross section for carrier capture by the parent state. The equilibrium carrier concentration was calculated as a function of temperature for each sample using known parameters for the band gap, the dopant ionization energy in Si, and the measured dopant concentration. All transitions involving loss of electrons or a site change were fit with a thermally activated rate,  $v_i$  or  $v_a = \rho \exp[-E/kT]$ , where  $E$  is the ionization or activation energy. The anisotropic hyperfine interaction of  $\text{Mu}_{\text{BC}}^0$  influences the spin dynamics in a way which modifies the temperature dependence of the visible  $\text{Mu}^\pm$  fraction arising from the  $\text{Mu}_{\text{BC}}^0$  precursor. Thus these effects had to be modeled in order to make proper reaction assignments and obtain correct dynamic parameters. The effects of the anisotropic  $\text{Mu}_{\text{BC}}^0$  spin dynamics on the polarization of subsequent states are presented in Appendix B. Finally, because of the hyperfine interaction, cyclic charge exchange involving ionization of muonium

and subsequent electron capture leads to the loss of muon polarization. At high temperature this charge cycle was found to involve  $\text{Mu}_{\text{BC}}^+$  and  $\text{Mu}_T^0$ .<sup>4</sup> Although the mechanism for the  $\text{Mu}_{\text{BC}}^+ \rightarrow \text{Mu}_T^0$  transition remains unclear, we have chosen to describe this process with a thermally activated capture rate  $v_{ac} = nv\kappa \exp[-E/kT]$ , where  $\kappa$  is the composite cross section and vibrational prefactor and  $E$  is the activation energy. We make no assumptions as to whether this represents two successive transitions or a single complex process. The transition from  $\text{Mu}_{\text{BC}}^0$  to  $\text{Mu}_T^-$  in  $n$ -type samples is treated in a similar manner.

The expression for the signal intensity, Eq. (6.1), with the polarization of the ionized muonium signal obtained from the three-state model described above was used to fit the normalized on-resonance diamagnetic rf asymmetry as a function of temperature between 10 and 500 K. In developing an interpretation of these results we started with a sample where the states and transition identities were well defined from earlier  $\mu\text{SR}$  experiments, then treated dynamic parameters from this sample as fixed in fitting or simulating the data from samples where additional processes were observed but not yet identified. We were eventually able to model all of the diamagnetic

TABLE II. Transitions identified for Mu in silicon along with the associated rf- $\mu\text{SR}$  feature used in fitting and modeling the resulting dynamic parameters. The transitions are discussed and their identification numbers are defined in Sec. II. The procedure used in fitting the data is described in Sec. VI.

Transition	rf Feature	Parameters
BC charge-state transitions:		
3: $\text{Mu}_{\text{BC}}^0 \rightarrow \text{Mu}_{\text{BC}}^+ + e^-$	<i>P</i> 11 140 K	$\rho_{\text{BC}}^{0/+} = 3.1 \times 10^{13} \text{ s}^{-1}$ $E_{\text{BC}}^{0/+} = 0.22 \pm 0.01 \text{ eV}$
4: $\text{Mu}_{\text{BC}}^0 + h^+ \rightarrow \text{Mu}_{\text{BC}}^+$	<i>P</i> 13 50 K	$\sigma_{\text{BC}}^{0/+} = 2.0 \times 10^{-15} \text{ cm}^2$
6: $\text{Mu}_{\text{BC}}^+ + e^- \rightarrow \text{Mu}_{\text{BC}}^0$	<i>N</i> 13 <sup>a</sup>	$\sigma_{\text{BC}}^{+/0} = 1.0 \times 10^{-15} \text{ cm}^2$
<i>T</i> charge-state transitions:		
2: $\text{Mu}_T^0 + e^- \rightarrow \text{Mu}_T^-$	<i>N</i> 15 50 K	$\sigma_T^{0/-} = 1.0 \times 10^{-15} \text{ cm}^2$
Site-change transitions:		
1: $\text{Mu}_T^0 \rightarrow \text{Mu}_{\text{BC}}^0$	<i>P</i> 11 270 K	$\rho_{T/\text{BC}}^0 = 9.5 \times 10^{12} \text{ s}^{-1}$ $E_{T/\text{BC}}^0 = 0.39 \pm 0.04 \text{ eV}$
Site-change and charge-state transitions:		
7: $\text{Mu}_{\text{BC}}^+ + e^- \rightarrow \text{Mu}_T^0$	<i>P</i> 11 to <i>N</i> 14 <sup>b</sup>	$\kappa_{\text{BC}/T}^{+/0} = 1.2 \times 10^{-10} \text{ cm}^2$ $E_{\text{BC}/T}^{+/0} = 0.38 \pm 0.06 \text{ eV}$
	<i>N</i> 15 340 K	$\kappa_{\text{BC}/T}^{+/0} = 0.7 \times 10^{-11} \text{ cm}^2$ $E_{\text{BC}/T}^{+/0} = 0.40 \pm 0.02 \text{ eV}$
5: $\text{Mu}_{\text{BC}}^0 + e^- \rightarrow \text{Mu}_T^-$	<i>N</i> 15 200 K	$\kappa_{\text{BC}/T}^{0/-} = 0.5 \times 10^{-9} \text{ cm}^2$ $E_{\text{BC}/T}^{0/-} = 0.34 \pm 0.01 \text{ eV}$

<sup>a</sup>The rf feature associated with this transition is the reduced amplitude of the  $\text{Mu}^+$  signal at room temperature.

<sup>b</sup>This transition is associated with the loss of the  $\text{Mu}^+$  amplitude seen in these samples at high temperature. The thermally activated cross section listed in the table is the number used in the displayed overall simulation. It is the average of the best-fit values for individual samples keeping the energy barrier fixed at 0.38 eV. The high-temperature drop of the diamagnetic amplitude in *N*15 was fit independently because, as was explained in the text, it can result from a similar processes as in the other samples but after a delay due to the higher  $n_e$  or from the thermal loss of an electron by  $\text{Mu}_T^-$ .

TABLE III. A list of the initial amplitudes used in fitting the  $\text{Mu}^\pm$  signal.

	<i>P</i> 15	<i>P</i> 14	<i>P</i> 13	<i>P</i> 11	<i>N</i> 12	<i>N</i> 13	<i>N</i> 14	<i>N</i> 15
$\text{Mu}_T^0$	0.08 <sup>a</sup>	0.07	0.26	0.46	0.49	0.54	0.21	0.17
$\text{Mu}_{\text{BC}}^0$	0.52	0.50	0.44	0.40	0.34	0.51	0.19 <sup>b</sup>	0.69
$\text{Mu}_{\text{BC}}^+$ or $\text{Mu}_T^-$	0.20	0.33	0.04	0	0	0.03	0.11	0.24
const <sup>c</sup>	0	0	0.05	0.03	0	0	0	0

<sup>a</sup>Since no data were obtained on this sample above room temperature, it is not possible to determine the initial amplitude of  $\text{Mu}_T^0$ . The number 0.08 is used only to draw the solid line in Fig. 6.

<sup>b</sup>The data taken on this sample are modeled without the charge-exchange cycle at the BC site, but with an initial amplitude of  $\text{Mu}_{\text{BC}}^0$  which only forms  $\text{Mu}_T^-$ .

<sup>c</sup>This is the fraction of muons stopped in the rf field but not in the Si samples.

data for Si with a single set of parameters by changing only the dopant concentration and sample orientation and varying the initial fractions; these are the solid curves shown in Fig. 6 and 7. The results of this overall fit are listed in Tables II and III; the samples used to extract the numbers associated with the various dynamic parameters are specified. In the following discussion each sample is treated in turn, transition process identification are detailed, and a number of consistency checks on state and process assignments are presented.

#### A. Intrinsic and *p*-type samples

We begin a detailed discussion of the data shown in Fig. 6 with the most nearly intrinsic case, a well-compensated slightly *p*-type sample (*P*11). At low temperatures only the states formed during the initial implantation are observed. Approximately equal fractions of  $\text{Mu}_{\text{BC}}^0$  and  $\text{Mu}_T^0$  are present, and the diamagnetic or ionized fraction is essentially zero. As the temperature is increased the first observed transition is indicated by the sharp increase in the amplitude of the diamagnetic signal near 140 K. This corresponds to ionization of  $\text{Mu}_{\text{BC}}^0$  to  $\text{Mu}_{\text{BC}}^+$ , whereby an electron is thermally promoted from the BC(+/0) level to the conduction band, process (3) as listed in Sec. II. This ionization process had been previously assigned based on the disappearance of the  $\text{Mu}_{\text{BC}}^0$  signals at essentially the same temperature in standard TFTD  $\mu\text{SR}$ .<sup>2</sup> Since the parent state  $\text{Mu}_{\text{BC}}^0$  has a highly anisotropic hyperfine interaction the effective magnetic field is in general not parallel to the applied field, and the spin dynamics are orientation dependent. As a result, the net polarization transferred to the ionized product has a complicated temperature dependence which is treated in Appendix B. Qualitatively, the anisotropy of  $\text{Mu}_{\text{BC}}^0$  is reflected in the rf data from this ionization process as a double step in the diamagnetic amplitude vs temperature (see Fig. 9). For this particular sample the lower-temperature step is well isolated from the  $\text{Mu}_T^0$  ionization discussed below, while the higher-temperature step overlaps this second ionization process. The component of the muon polarization parallel to the effective field is time independent and does not contribute to depolarization, hence formation of  $\text{Mu}_{\text{BC}}^+$  can be detected immedi-

ately. However, due to dephasing for the perpendicular component, the ionization must be rapid compared to the  $\mu\text{SR}$  frequencies of  $\text{Mu}_{\text{BC}}^0$  before the full signal from the ionized final state can be observed. This is a consequence of random transition times and the associated precessional phase of the initial state, similar to the lifetime broadening and dephasing effects in TFTD methods. The relative strength of the two steps depends on sample orientation: for the  $\langle 110 \rangle$ -oriented *P*11 sample the ratio is about 4 to 1. When these anisotropy effects are properly modeled these data yield a best-fit energy value of  $E_{\text{BC}}^{0/+} = 0.22$  eV for ionization of  $\text{Mu}_{\text{BC}}^0$ , locating the position of the BC(+/0) level relative to the conduction-band edge. We note that parameters from the older TFTD data<sup>2</sup> mentioned in Sec. II with an energy of 0.17 eV provide a visually satisfactory simulation for this process. However, the rf- $\mu\text{SR}$  data yield a fully independent determination of this and other parameters. Further comparisons with other measurements will be discussed in below.

The second process to become active with increasing temperature shows up as a gradual increase in the diamagnetic signal and is centered near 270 K, approximately where  $\text{Mu}_T^0$  is known to ionize from earlier TFTD data. At room temperature most of the muons are accounted for in the  $\text{Mu}^\pm$  signal. Decay positron channeling studies<sup>16</sup> have shown this to be a muon at the BC site, implying a  $\text{Mu}_{\text{BC}}^+$  final state based on the theoretical considerations discussed above. Within the dynamic model of Sec. II the disappearance of  $\text{Mu}_T^0$  must then be due to a site change as neutral  $\text{Mu}^0$ , listed as process (1). However, since the rate for ionization at the BC site is now very rapid the  $e^-$  is quickly lost and the intermediate  $\text{Mu}_{\text{BC}}^0$  state is not observed. Under these conditions the site change will constitute the rate-limiting step for the  $\text{Mu}_T^0$  ionization. The resulting best-fit energy parameter yields  $E_{T/\text{BC}}^0 = 0.39$  eV for the *T* to BC site-change barrier for  $\text{Mu}^0$ . Note that this is not just a matter of fitting the region from 200 to 300 K by varying the  $\text{Mu}_T^0$  site-change rate since the  $\text{Mu}_{\text{BC}}^0$  ionization makes a contribution in this temperature region, as discussed in the preceding paragraph.

Above room temperature, cyclic electron capture and ionization results in the loss of the  $\text{Mu}^\pm$  signal. If one assumes a fixed BC position during this cyclic  $e^-$  exchange,

one cannot reproduce the observed rate of diamagnetic signal loss with increasing temperature. All relevant parameters except for the capture cross section are known from earlier data or other rf features, and their use in a single-parameter fit forces a much slower loss of diamagnetic intensity with increasing temperature. Simulations using the larger hyperfine parameter and slower ionization rate of  $\text{Mu}_T^0$  in place of the  $\text{Mu}_{\text{BC}}^0$  parameters leads us to conclude that such a sharp drop can result if the neutral center is  $\text{Mu}_T^0$ . Recent LF measurements<sup>4</sup> also identify a  $\text{Mu}_T^0$ -like state as the active relaxing species above 450 K, consistent with this conclusion. Furthermore, electron capture at the BC site is unlikely to lead to a site change because the barrier for  $\text{Mu}^0$  to return to the  $T$  site is larger than the 0.39-eV  $T \rightarrow \text{BC}$  barrier by  $\Delta$ , theoretically estimated to be a few tenths of an eV,<sup>15</sup> yielding a rather slow transition rate. In contrast, the  $\text{Mu}_{\text{BC}}^0$  ionization rate becomes very rapid at these temperatures, completely dominating any other route out of  $\text{Mu}_{\text{BC}}^0$  for  $p$ -type samples. A direct transition from  $\text{Mu}_{\text{BC}}^+$  to  $\text{Mu}_T^0$  [process (7)] is therefore required, labeled in our notation as activated capture or a composite site-change–electron-capture process. A fit to the  $P11$  data yields an energy parameter of  $E_{\text{BC}/T}^{+/0} = 0.38$  eV with roughly 15% errors. The composite cross section and vibrational prefactor ( $\kappa_{\text{BC}/T}^{+/0}$ ) used in the displayed overall fit is an average of best-fit values for individual samples keeping this barrier fixed. These data imply a site change as part of the onset of the high-temperature charge cycle, but do not directly characterize the processes involved above roughly 450 K where essentially all of the longitudinal depolarization data on this cycle were obtained.

We now discuss results for the more heavily doped  $p$ -type Si:B samples  $P13$  and  $P14$  (Fig. 6). Two additional features appear at low temperature: the initial diamagnetic fraction increases with the dopant concentration, and another step appears at about 50 K. The increase in initial diamagnetic amplitude is attributed to ionization of the B dopants from thermalization of the energetic  $\mu^+$  during implantation. A possible interpretation is that the increased density and capture of excess holes within the stopping spur simply reduces the  $\text{Mu}^0$  formation probability in favor of  $\text{Mu}_{\text{BC}}^+$ . However, when initial-state fractions produced by the fit are compared with the  $P11$  sample, it is obvious that the increase in diamagnetic amplitude comes at the expense of  $\text{Mu}_T^0$ . It is also clear that  $\text{Mu}_T^0$  remains the prompt state since the  $\text{Mu}_T^0$  rf signal in the  $P14$  sample, the dashed line in Fig. 6, is still quite strong at low temperatures. The rf sensitivity allows a range of relatively fast reaction times for which both states, the prompt  $\text{Mu}_T^0$  and delayed  $\text{Mu}_{\text{BC}}^+$ , are visible in the time-integral measurement. The precise nature of this low-temperature diamagnetic state and the reaction sequence leading to it are not yet clear. The process may involve an interaction between the rapidly diffusing  $\text{Mu}_T^0$  and the boron dopants. One possibility is the reaction  $\text{Mu}_T^0 + \text{B}^0 \rightarrow \text{Mu}_{\text{BC}}^+ + \text{B}^-$ . If  $\text{Mu}_T^0$  diffusion is sufficiently slowed by the strain field associated with the impurity, then the final BC position should not be far from the boron as a result of such a process. If the muon were to end up next to the boron, the result

would be the illusive muonium analog of the hydrogen-boron passivation complex.<sup>1</sup>

The second feature, the increase in the amplitude at 50 K, occurs in the temperature region where the B impurities ionize. Because of the rapid growth in  $h^+$  concentration with increasing temperature from such acceptor ionization, the 50-K increase in  $\text{Mu}^\pm$  rf- $\mu\text{SR}$  signal intensity is assigned to hole capture by  $\text{Mu}_{\text{BC}}^0$ , or process (4). Adding this transition to the model yields a single extra parameter,  $\sigma_{\text{BC}}^{0/+}$  representing the cross section for  $h^+$  capture by  $\text{Mu}_{\text{BC}}^0$ . When fitting the rf data for the  $P13$  sample the ionization and site-change parameters were fixed to values obtained from the  $P11$  sample, while the initial-state fractions were allowed to vary along with  $\sigma_{\text{BC}}^{0/+}$ . The cross section ( $\sigma_{\text{BC}}^{0/+}$ ) was then also fixed for the  $P14$  sample to the  $P13$  value. This procedure satisfactorily reproduces observed features analogous to those in the  $P11$  sample as well as the step at 50 K. We then checked for consistency by including the hole capture process for  $P11$ , and no visible step was produced at 50 K for that sample because of the low hole concentration. Note that both the thermal ionization of  $\text{Mu}_{\text{BC}}^0$  and hole capture process described above will produce two steps in the recovered diamagnetic amplitude since the  $\text{Mu}_{\text{BC}}^0$  parent state is responsible in both cases. For the  $P13$  and  $P14$  samples the  $\text{Mu}_{\text{BC}}^0 \rightarrow \text{Mu}_{\text{BC}}^+$  state change is due to a combination of  $h^+$  capture and electron thermal ionization. The  $P14$  sample has a  $\langle 100 \rangle$  orientation, which modifies the two steps as compared to that discussed for  $P11$ , yielding two components of equal strength showing up at 50 and 200 K. The  $P14$   $\text{Mu}_T^0$  fraction is almost entirely converted to a diamagnetic state by the very fast interactions with acceptors discussed above. These interactions are visible in the rf data as the increased initial (low-temperature) diamagnetic fraction. Only the very small increase above 200 K in the  $P14$  data is related to the site change and ionization processes (1) and (3) as assigned for the initial  $\text{Mu}_T^0$  fraction in  $P11$ .

In order to double check our identification of the 50-K features in the doped materials, we examined two samples with other dopants having different acceptor levels, Ga and In which are located at 72 and 160 meV above the valence-band edge as compared to 44.5 meV for B in Si. In each case the expected shift of the step associated with acceptor ionization and  $h^+$  capture was observed, confirming this process as involving thermal ionization of the acceptor hole. Figure 6 shows the low-temperature rf- $\mu\text{SR}$  data and calculated curve for the  $\text{Mu}_{\text{BC}}^+$  state in the Ga-doped sample  $P15$ . The shift of the dopant ionization and subsequent  $\text{Mu}_{\text{BC}}^0 + h^+ \rightarrow \text{Mu}_{\text{BC}}^+$  hole capture process (4) to higher temperatures with increasing hole ionization energy is clearly displayed.

Above room temperature all of the  $p$ -type samples show a rapid decrease in diamagnetic amplitude with increasing temperature. Comparison of the heavily doped sample  $P14$  with the nearly intrinsic  $P11$  clearly indicates a shift in the temperature at which the drop begins. The shift to higher temperatures for more heavily doped  $p$ -type samples implies that the charge-exchange cycle involves conduction electrons rather than holes, reinforcing similar evidence from LF data<sup>14</sup> on doped samples.

### B. The $n$ -type samples

Data on  $n$ -type samples are considerably more complicated than for the  $p$ -type cases just discussed because a fourth state,  $\text{Mu}_T^-$ , becomes important. The presence of  $\text{Mu}_T^-$  implies that several additional transition processes may also become active, specifically (2), (5), and (8) from the list in Sec. II. The data on  $n$ -type samples below room temperature are also modified by extra depolarization mechanisms; these are spin-flip scattering of conduction electrons from neutral muonium centers and a low-temperature charge-state cycle at the individual BC site, none of which are important in  $p$ -type materials. All of the processes we observed in the  $p$ -type samples are still present, although their effective temperature ranges are shifted by the change in extrinsic carrier type and the associated increase in  $e^-$  capture rates. One should again note that for  $n$ -type samples the Fermi level lies above both muonium levels in the gap, so that the equilibrium populations favor  $\text{Mu}_T^-$  and  $\text{Mu}_{\text{BC}}^0$  at the respective sites, as opposed to  $\text{Mu}_T^0$  and  $\text{Mu}_{\text{BC}}^+$  for intrinsic and  $p$ -type materials.

A detailed discussion of the  $n$ -type samples begins with the phosphorous-doped sample  $N15$  (Fig. 7), from which most of the additional dynamic parameters were derived. Starting from the lowest temperatures, the relatively high initial diamagnetic amplitude is attributed to the ionization of P dopants during thermalization of the energetic  $\mu^+$  in a rapid carrier capture process similar to that discussed for the  $p$ -type samples. Either two electrons are captured during the initial stopping processes, or a slightly delayed interaction between the highly mobile  $\text{Mu}_T^0$  and  $\text{P}^0$  results in exchange of an electron yielding  $\text{P}^+$  and  $\text{Mu}_T^-$ .

The next visible feature with rising temperature is the increase in diamagnetic amplitude at 50 K, corresponding to the temperature at which P thermally ionizes. The P donor level is located at 45.5 meV below the conduction-band edge. The 50-K feature is thus attributed to electron capture by  $\text{Mu}_T^0$ , listed as process (2). Fitting this step yields  $\sigma_T^{0/-}$ , the cross section for electron capture by  $\text{Mu}_T^0$ . The data and process modeling indicate that above 100 K essentially all of the initial  $\text{Mu}_T^0$  fraction has formed  $\text{Mu}_T^-$  for this sample. Even though the drop in  $\text{Mu}_{\text{BC}}^0$  amplitude at 50 K, the dotted line for  $N15$  in Fig. 7, appears to be correlated with the increase in the diamagnetic signal strength, LF depolarization measurements<sup>20</sup> in this sample demonstrate that the neutral BC center remains present up to roughly 200 K. However, it is involved in spin-flip scattering of conduction electrons giving rise to significant relaxation of the muon spin polarization. Therefore, the loss of the  $\text{Mu}_{\text{BC}}^0$  signal in the rf- $\mu$ SR data is due to depolarization arising from this spin-flip scattering rather than a change in the muonium state. Specifically, this scattering is a spin-exchange process in which the muonium electron spin and a conduction electron flip. The change of the Mu electron-spin state is subsequently transferred to the muon via the hyperfine interaction, resulting in loss of muon polarization in a manner very similar to that for the rapid  $e^-$  capture-ionization charge-exchange cycle at

higher temperatures. The primary effect of this scattering process is loss of the  $\text{Mu}_{\text{BC}}^0$  signal at low temperature. Even if  $\text{Mu}_{\text{BC}}^0$  were to thermally ionize with the  $e^-$  promoted to the conduction band, it will immediately recapture another  $e^-$  and return to the BC neutral state [process (6)] because of the high  $e^-$  density. The resulting very short-lived  $\text{Mu}_{\text{BC}}^+$  state will not show up in the diamagnetic signal. The only effect of a charge-exchange cycle at the BC site on the rf- $\mu$ SR data at high donor concentrations is an additional increase in the depolarization rate for  $\text{Mu}_{\text{BC}}^0$ . Such rate changes associated with ionization of  $\text{Mu}_{\text{BC}}^0$  are indeed observed in LF relaxation data on several  $n$ -type samples.<sup>20</sup>

The sharp step at 200 K is assigned to a BC to  $T$  site change which takes place sufficiently rapidly at these temperatures so that the polarization from the  $\text{Mu}_{\text{BC}}^0$  parent is maintained. We have identified this as a combined electron capture and site change leading to  $\text{Mu}_T^-$ , i.e., process (5), and obtained an energy parameter ( $E_{\text{BC}/T}^{0/-}$ ) of  $0.34 \pm 0.01$  eV for the process.  $N15$  is a  $\langle 100 \rangle$ -oriented sample; therefore, only the half of  $\text{Mu}_{\text{BC}}^0$  polarization parallel to the effective field is recovered in the  $\text{Mu}_T^-$  signal. The other half, which normally would be recovered at higher temperature, overlaps with the drop in signal related to the high-temperature electron exchange cycle. In all the  $n$ -type samples at sufficiently high temperatures the diamagnetic state appears to be  $\text{Mu}_{\text{BC}}^+$  as in intrinsic and  $p$ -type materials. It is possible to obtain rough estimates of the temperature at which the identity of the diamagnetic state switches for each sample by comparing the electron-capture rate by  $\text{Mu}_T^0$  to the rate for the  $T \rightarrow \text{BC}$  site change and subsequent ionization to  $\text{Mu}_{\text{BC}}^+$  (a comparison for  $N13$  is shown in Fig. 8 and discussed below). This temperature is found to be around 350 K for  $N15$ . Because  $\text{Mu}_T^-$  is present in this

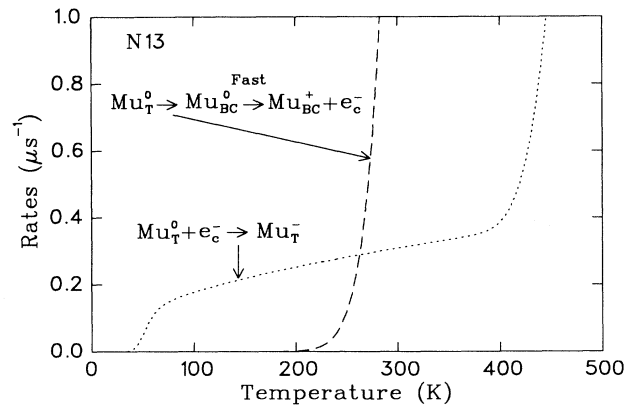


FIG. 8. Rate comparison for the electron-capture vs site-change transitions out of  $\text{Mu}_T^0$  for  $N13$ . When the  $T \rightarrow \text{BC}$  site change dominates, the diamagnetic state from the initial  $\text{Mu}_T^0$  fraction becomes  $\text{Mu}_{\text{BC}}^+$  rather than  $\text{Mu}_T^-$ . Similar comparisons for other samples and transitions were used to verify state and transition assignments.

sample to above room temperature, the temperature at which the diamagnetic amplitude begins to decrease is higher than for sample *N14*. This reverses the observed trend for lower donor concentrations that the temperature at which the diamagnetic amplitude drops decreases as the donor concentration increases and raises some questions as to whether the controlling process is identical or not. The systematics of this amplitude drop in the *n*-type samples will be discussed in more detail after examining the lower-temperature behavior in each sample.

The temperature dependence of the normalized diamagnetic asymmetry measured in a more heavily *P*-doped sample *N16* is very similar to the *N15* data, with the exception of a broader plateau around room temperature. This is consistent with the fact that heavier *n*-type doping increases the transition rate to  $\text{Mu}_T^-$  [processes (2) and (5)]. Because of the heavy doping the rf heating of this sample was a serious problem, resulting in a large uncertainty in the measured temperature. The *N16* data are therefore omitted from Fig. 7.

We now discuss the two intermediate concentration *n*-type samples, *N13* and *N14* (Fig. 7). For both samples the rise in the diamagnetic signal strength at 50 K is associated with donor ionization and subsequent capture of an electron by the  $\text{Mu}_T^0$  state to form  $\text{Mu}_T^-$ . The *N13* and *N14* data are reproduced quite accurately in this region using the parameters from *N15*. Simulations using the parameters extracted from the  $\text{Mu}_{\text{BC}}^0$  to  $\text{Mu}_T^-$  activated capture process for *N15* identify the step just above 200 K in *N14* and the initial part of the rise in *N13* as due to the same source: process (5), the combined  $\text{BC} \rightarrow T$  site change and  $e^-$  capture. Above about 250 K in *N13* the remaining increase in the diamagnetic signal is assigned to the  $T \rightarrow \text{BC}$  site change for  $\text{Mu}^0$  followed by ionization; the same process as for the near intrinsic and *p*-type samples. Comparison of the rates for the two competing  $\text{Mu}_T^0$  loss routes, process (2) and processes (1) and (3), using the *N15* parameters yields the change in diamagnetic state for *N13* near 250 K (see Fig. 8). Also, at roughly 250 K the slope of the  $\text{Mu}^\pm$  amplitude versus temperature changes for *N13*, this is taken to indicate a change in the identity of the ionized state from predominantly  $\text{Mu}_T^-$  at lower temperatures to primarily  $\text{Mu}_{\text{BC}}^+$  at higher temperatures.

The spin-exchange scattering process discussed in connection with *N15* will remain active at lower electron concentrations. The resulting  $\text{Mu}_{\text{BC}}^0$  depolarization is seen as a decreasing amplitude and a broader linewidth of the rf signal from that state below the  $\text{Mu}_{\text{BC}}^0$  ionization temperature. As mentioned above, LF data for *N13* and *N14* confirm the presence of this process, and show a rapid increase in the polarization loss rate when the BC state ionizes between 140 and 160 K.<sup>20</sup> The increased depolarization due to charge exchange at the BC site [processes (3) and (6)] reduces the rf amplitude for the diamagnetic signal in *N13*, providing a rough value for the electron capture cross section at the BC site  $\sigma_{\text{BC}}^{+/0}$ . Charge exchange at the BC site is more important in the *n* than in the *p*-type samples as a consequence of the much faster electron-capture rate, again confirming an  $e^-$  rather than a  $h^+$  process. In *N14* the maximum amplitude of the ob-

served  $\text{Mu}^\pm$  state is the lowest of any sample we examined. We attribute this to a combination of spin-exchange scattering of conduction electrons from  $\text{Mu}_{\text{BC}}^0$  (above 50 K), cyclic charge exchange at the BC site (above 150 K), and the high-temperature charge-exchange cycle involving  $\text{Mu}_T^0$  which for this sample sets in just below room temperature. The LF relaxation rates confirm the presence of each of these processes. A full quantitative treatment of the data on these intermediate concentration *n*-type samples requires a four-state model with all of the depolarization processes properly included. Qualitatively, the important contributions are identified by the present incomplete treatment.

Finally we turn to the low-temperature data for the remaining case *N12*, which is the most nearly intrinsic of the *n*-type samples (Fig. 7). All of the features in the *N12* data arise from the same transitions as for the near intrinsic *p*-type sample *P11*. With the exception of the  $\text{Mu}_{\text{BC}}^0$  ionization step just above 150 K, parameters taken from *P11* do a reasonable job reproducing the *N12* data. The most glaring problem with the whole set of data as related to our model occurs for the  $\text{Mu}_{\text{BC}}^0$  ionization step in this sample. The solid line, which represents the results for our model with parameters extracted from the *P11* sample, clearly does not reproduce the data from 150 to 230 K. The rf- $\mu$ SR amplitude of the  $\text{Mu}_{\text{BC}}^0$  state does drop abruptly near 150 K as expected for the ionization process. We attempted unsuccessfully to model the 30-K offset between the temperature at which  $\text{Mu}_{\text{BC}}^0$  ionizes in the *p*-doped samples and the recovered  $\text{Mu}^\pm$  signal in *N12* by using a charge-exchange cycle at the BC site. A capture cross section sufficiently large to reproduce the observed temperature shift and slope results in very rapid depolarization and essentially zero amplitude for the rf signal as well. Inclusion of another depolarization mechanism in addition to transitions between states will solve this difficulty; however, such a treatment is beyond the present model. Spin-exchange scattering by conduction electrons provides such a mechanism, but the few LF relaxation data points we have for this sample suggest that the rates may be too small to fully account for the observed effects.

The high-temperature charge cycle in the *N12*, *N13*, and *N14* samples has been assigned to the same complex set of transitions identified for the *p*-type materials. The drop in the diamagnetic amplitude is assigned to the  $\text{Mu}_{\text{BC}}^+ \rightarrow \text{Mu}_T^0$  activated-capture process (7) described earlier. The decrease in amplitude for these samples was modeled using the parameters from *P11* along with the appropriate carrier densities, which satisfactorily reproduces both the shifts in onset temperature and the changes in slope. Up to *N14* the shift is to lower temperature compared to *P11*, consistent with the previous conclusion that the charge exchange involves conduction electrons. Simulating the high-temperature drop in the *n*-type data up to *N14* by using the *P11* parameters is also consistent with the change in the diamagnetic charge state from mainly  $\text{Mu}_T^-$  to mostly  $\text{Mu}_{\text{BC}}^+$  occurring below the temperature at which charge exchange becomes active. The shift of the drop in the amplitude to higher temperature for *N15* and *N16* compared to the

lower concentration samples can result either from delayed access to the  $\text{Mu}_{\text{BC}}^+$  state because the capture rate to  $\text{Mu}_T^-$  is faster than the ionization rate, or from a large energy parameter to describe the thermal loss of an electron by  $\text{Mu}_T^-$ , i.e., the depth of the  $\text{Mu}_T(0/-)$  energy level below the conduction band. Assuming delayed formation of  $\text{Mu}_{\text{BC}}^+$ , and independently fitting this feature for the *N15* sample, yields an energy barrier of  $E_{\text{BC}/T}^{+/0} = 0.40 \pm 0.02$  eV and  $\kappa_{\text{BC}/T}^{+/0} = 0.7 \times 10^{-11}$  cm<sup>2</sup>. This energy is consistent with the value of  $E_{\text{BC}/T}^{+/0}$  from *P11* and the shift of the drop in amplitude to higher temperature produces the small value of  $\kappa_{\text{BC}/T}^{+/0}$  reflecting delayed formation of  $\text{Mu}_{\text{BC}}^+$  in this interpretation. If the drop results from the breakup of  $\text{Mu}_T^-$  and subsequent charge exchange then, based on the fit result and observed stability of  $\text{Mu}_T^-$ , an estimate of the energy parameter places the  $T(0/-)$  level deeper than 0.4 eV relative to the conduction-band edge. Since all possible reaction paths are not included in the current model, resolution of this important issue must await the development of a more complete theoretical model and reanalysis of the data, as well as additional measurements of intermediate and heavily doped *n*-type samples. In Fig. 7, Table II, and Table III we display results obtained from modeling the *n*-type data.

In attempting to find a single set of parameters that describe the muonium dynamics in all the samples, we have examined the data from each sample by freeing either the prefactors or energies to improve the individual fit. While this procedure improves Figs. 6 and 7, we selected a single set of parameters (Table II) that satisfactorily reproduce all of the features. Most parameters are from *P11* and *N15* because the features and corresponding transitions are well separated in these samples, and the resulting parameters are reasonably well determined. The main adjustment made to parameters obtained from these two samples was for the activated capture part of the high-temperature charge cycle. For that specific transition for all samples except *N15* we used  $\kappa_{\text{BC}/T}^{+/0}$ , which is an average of values obtained in individual sample fits with the barrier fixed to the *P11* value. Two additional capture cross sections were derived from data on other samples since the two primary ones were insensitive to those processes. The three-state model and the parameter selection procedure described above work very well for the *p*-type samples. In modified form with  $\text{Mu}_T^-$  in place of  $\text{Mu}_{\text{BC}}^+$ , this treatment also works satisfactorily for the more heavily doped *n*-type samples at low temperatures. All four states are involved in the *n*-type samples, with maximum overlap of the two charged states occurring for intermediate electron densities. The presence of extra depolarization mechanisms in *n*-type samples further complicates the model. Nevertheless, the three-state model describes the *N15* data below room temperature very well because only three states are present,  $\text{Mu}_T^-$  and the two paramagnetic states. The more complete four-state model will be required to describe fully the dynamics particularly in *n*-type material. Before such a model can be implemented it is crucial to understand the details of the switch in diamagnetic state identity and the

formation of initial fractions. This problem is made more difficult by the fact that  $\text{Mu}_T^-$  and  $\text{Mu}_{\text{BC}}^+$  produce the same rf- $\mu$ SR and conventional  $\mu$ SR signals. While longitudinal relaxation data provide some help as a consistency check, the two ionized states still cannot be separated. An experimental check of ionization assignments in the *n*-type samples may soon be possible using the microwave spectrometer<sup>21</sup> to measure the temperature dependence of the  $\text{Mu}_T^0$  and  $\text{Mu}_{\text{BC}}^0$  amplitudes. With the higher microwave frequencies, spectral lines from  $\text{Mu}_{\text{BC}}^0$  are less sensitive to the spin-flip scattering, which causes severe broadening in the current rf data for higher doping levels. The  $\text{Mu}_T^0$  signals have so far been observed in *n*-type samples only at microwave frequencies.

### C. Identification of ionized states and transition processes

The question of detailed  $\text{Mu}^\pm$  identifications were deferred at several points in the preceding discussion. The starting point in these state assignments involve general qualitative arguments regarding parent states and expected transitions under various conditions of carrier densities and temperature. Following tentative state and transition assignments, dynamic parameters were extracted and compared for several samples. Changes in slopes or other identifiable features in the data were used as a guide in determining where the charged state might change or where there was a change in the active transition. Finally, comparison of relative rates for competing transitions out of a given state using the extracted parameters were used to check for consistency in the overall model. Tables II and III provide a full listing of the parameters used to produce the solid curves in Figs. 6 and 7. This set was selected to give the best overall fit to the full data set rather than to provide the best parameters for any given sample or transition process.

In *n*-type samples a rate comparison for  $\text{Mu}_T^0 \rightarrow \text{Mu}_T^-$  and  $\text{Mu}_T^0 \rightarrow \text{Mu}_{\text{BC}}^0$  helps identify the  $\text{Mu}^-$  to  $\text{Mu}^+$  crossover point for ionized states arising from the  $\text{Mu}_T^0$  precursor. The  $T$  to BC site change leads quickly to  $\text{Mu}_{\text{BC}}^+$  with some polarization loss from the BC(+/0) charge cycle. The temperature at which these two rates cross is a lower limit on the  $\text{Mu}^-$  to  $\text{Mu}^+$  diamagnetic state crossover point. Figure 8 displays this rate comparison for the *N13* sample. The rate for the site change dominates above 240 or 250 K, consistent with our assignment of the charged-state switch point to the slope change at 250 K in the *N13* data (see Fig. 7). Similar comparisons of relative rates were carried out for each *n*-type sample to verify ionized state identity, and were also used to check the transition assignments. These consistency checks indicate that the overall model holds together very well. Because a number of the energy parameters have very similar values, rate checks on the most likely transition paths proved to be an extremely valuable identification tool for matching observed features with the responsible processes.

## VII. COMPARISON TO H DYNAMICS

Since muonium and hydrogen form many of the same defects in semiconductors, a comparison of our results for the Mu dynamics with the few existing measurements for isolated H in Si is pertinent. One can expect that purely electronic transitions should have nearly identical energy parameters for these essentially identical defects. Values for energy barriers to motion of the nuclei (proton or muon) are expected to be lower for Mu than for H undergoing the same motion due to the mass differences and resulting increase in zero-point kinetic energy for Mu. There are only a few experimental energy measurements for H which are directly comparable. All involve  $H_{BC}^0$ , which is the only isolated H impurity directly observed and unambiguously identified.

The  $E3'$  deep-level transient spectroscopy (DLTS) line has been identified with the hydrogen  $BC(+/0)$  energy level and the depth below the conduction-band edge measured at  $0.164 \pm 0.011$  eV.<sup>22</sup> This number agrees very well with the  $0.168 \pm 0.013$  eV value extracted from the  $T_2^{-1}$  measurements on Mu\* some years ago.<sup>2</sup> The rf- $\mu$ SR number obtained from the  $P11$  data is somewhat higher at  $0.22 \pm 0.01$  eV, with the error obtained assuming no parameter correlations; a more realistic error is roughly three times larger. We have already noted that the earlier  $\mu$ SR parameters give a good simulation of the rf results for this transition; however, proper inclusion of the anisotropic spin dynamics in the subsequent fitting increased the ionization energy to the value reported here. The recoverable loss of the intensity of the  $AA9$  electron paramagnetic resonance (EPR) spectrum from  $H_{BC}^0$  (Ref. 11) has also been reproduced using the DLTS ionization parameters.<sup>23</sup> With an increased error estimate for the current muonium rf results, all of these measurements come close to overlapping. It would thus seem appropriate to accept the two closely agreeing H and Mu values as the best determination of this level depth.

The other two energy parameters available from the hydrogen work are for the processes we identify as activated capture or combined  $e^-$  capture and BC to  $T$  site changes. These transitions lead from  $H_{BC}^+$  to  $H_T^0$  and from  $H_{BC}^0$  to  $H_T^-$  in the dynamic model we have developed from the Mu results. For the  $Mu_{BC}^+ \rightarrow Mu_T^0$  transition [process (7)] we obtain an energy of  $E_{BC/T}^{+/0} = 0.38 \pm 0.06$  eV from the charge cycle in the  $P11$  sample. For the analogous H transition a value of  $0.44 \pm 0.01$  eV was reported from the DLTS work,<sup>22</sup> and  $0.48 \pm 0.04$  eV was obtained from the EPR studies.<sup>24</sup> Both of the H numbers come from annealing studies and rely on establishing equilibrium over a time frame ( $\approx 300$  s) about eight orders of magnitude longer than the few- $\mu$ s time scale of the nonequilibrium  $\mu$ SR measurements. These values are consistent with the expected increase in barrier height for H motions relative to barriers for the lighter Mu as a consequence of their different zero-point energies.

The other activated capture transition  $Mu_{BC}^0 \rightarrow Mu_T^-$  [process (5)] poses a more complicated comparison problem. The Mu data come from the 200-K step in the  $n$ -type samples which does not permit a clean determina-

tion of the actual barrier due to complications arising from the rapid depolarization of the  $Mu_{BC}^0$  parent state from spin-flip scattering of conduction electrons. This will result in an overestimate of the true barrier, unless the depolarization rates are properly included in the model, which was not possible using our analytical treatment. Further, LF relaxation data, from which the depolarization rates could be extracted, are not complete; thus only estimates are available for most samples. The Mu and H measurements yield  $E_{BC/T}^{0/-} = 0.34 \pm 0.01$  eV from the rf- $\mu$ SR data as compared to  $0.293 \pm 0.003$  eV from DLTS annealing curves for  $^1H$  and  $0.30 \pm 0.01$  eV for  $^2H$  when the prefactors are forced to have the proper ratio.<sup>22</sup> Since the depolarization effects in the Mu data would lower the 0.34-eV value, these numbers appear to be in fairly good agreement. Assuming that the potential wells within which the BC species reside have the same shapes in all cases (H vs Mu as well as neutral vs positive charge states) the H–Mu barrier differences should be very similar for these two  $BC \rightarrow T$  activated-capture site-change transitions, i.e., processes (7) and (5).

The overall agreement of the Mu and H measurements of these energy parameters when expected real differences are taken into account appears to be quite good. The muonium results presented here help to clarify the hydrogen data and verify the general picture and transition assignments arrived at from the DLTS and EPR annealing studies. This general agreement of  $Mu_{BC}^0$  and  $H_{BC}^0$  dynamic behavior implies that there should be similar agreement with respect to the remaining states and transitions, none of which have been directly observed for hydrogen. The full dynamic model developed as a result of the LF relaxation and rf- $\mu$ SR studies of the muonium analog of isolated H impurities in silicon should be at least qualitatively correct for hydrogen. One of the important consequences of this work should be a caution to researchers working on hydrogen diffusion and other dynamic properties that a complicated set of state changes are active on short-time scales within the temperature range usually investigated. Results which are implicitly based on an assumption of a single diffusing hydrogen state, without consideration of possible involvement of other sites or charge states, should be reexamined on the basis of this more complete dynamic model.

## VIII. CONCLUSIONS

We have investigated the dynamics of muonium site and charge-state transitions in silicon using rf- $\mu$ SR techniques supplemented by longitudinal depolarization measurements. Data from the rf- $\mu$ SR studies of five  $p$ -type and five  $n$ -type samples have led to the development of a quantitative dynamic model of the behavior of Mu in Si. Dynamic parameters are obtained for most of the transitions. Parameters from fits to single samples particularly sensitive to each process provide an excellent simulation of the data for all other samples spanning a broad range of doping concentrations. Comparisons of the relative rates for competing transitions verify that our process assignments are fully consistent. Inclusion of transitions not observed in a given sample show that the related

features should not appear. These checks provide strong evidence that the overall model is self-consistent and that the process assignments are correct. The addition of a  $\text{Mu}^-$  state and its transitions together with the extra depolarization mechanism involving conduction electrons make the interpretation of the data for  $n$ -type samples considerably more complex than for the  $p$ -type ones. The results of longitudinal relaxation measurements were used in addition to the rf- $\mu$ SR measurements to qualitatively understand the  $n$ -type data and to help identify or verify transition processes. The final result is a complete dynamic model for isolated Mu impurities in Si with an initial set of parameters for all but one of the relevant transition processes. The remaining undetermined energy parameter would locate the  $T(0/-)$  energy level relative to the conduction-band edge. Based on the observed stability of  $\text{Mu}_T^-$  in heavily doped  $n$ -type samples, a very crude estimate places this level deeper than approximately 0.4 eV, which would support arguments in favor of Mu or H forming a negative- $U$  system in silicon.

The overall dynamic model is expected to be at least qualitatively correct for hydrogen impurities in silicon, as well as for muonium, and provides semiquantitative information about H dynamics. Comparison of our parameters for Mu transition processes with the few analogous measurements for hydrogen show quite good agreement when expected real differences related to zero-point energies are taken into account. These data show that a complicated set of site changes and charge-state transitions are active on a very short-time scale compared to measurement times for most experimental determinations of diffusion-related parameters for hydrogen. This in turn implies that assumptions of a single diffusing hydrogen state need to be reexamined in interpreting much of the existing H data.

#### ACKNOWLEDGMENTS

We would like to thank M. Thewalt for characterizing the samples with photoluminescence. It is also a pleasure to thank S. F. J. Cox, J. W. Schneider, D. W. Cooke, S. A. Dodds, R. C. DuVarney, S. K. Estreicher, C. D. Lamp, P. Mendels, and T. Pfiz for valuable discussions and/or experimental assistance. This work is partially supported by grants from the Natural Sciences and Engineering Research Council of Canada, the Robert A. Welch Foundation [C-1048 (T.L.E.), D-1053 (R.L.L.)] and the U.S. National Science Foundation [DMR-8917639 and DMR-9220521 (T.L.E. and B.H.)].

#### APPENDIX A: THE THREE-STATE STRONG COLLISIONAL MODEL

The muonium states in  $p$ -type samples are

$$\text{Mu}_{\text{BC}}^+, \text{Mu}_{\text{BC}}^0 \text{ and } \text{Mu}_T^0.$$

Processes involving the  $\text{Mu}_{\text{BC}}^+$  state discussed in Sec. II

and Fig. 1(c) are as follows.

Process (1):  $\text{Mu}_T^0 \xrightarrow{\nu_a} \text{Mu}_{\text{BC}}^0$ :  $\nu_a = \rho_{T/\text{BC}}^0 \exp[-E_{T/\text{BC}}^0/kT]$  is the site change rate.

Process (3):  $\text{Mu}_{\text{BC}}^0 \xrightarrow{\nu_i} \text{Mu}_{\text{BC}}^+ + e_c^-$ :  $\nu_i = \rho_{\text{BC}}^{0/+} \times \exp[-E_{\text{BC}}^{0/+}/kT]$  is the ionization rate.

Process (6):  $\text{Mu}_{\text{BC}}^+ + e_c^- \xrightarrow{\nu_c} \text{Mu}_{\text{BC}}^0$ :  $\nu_c = n_e v_e \sigma_{\text{BC}}^{+/0}$  is the rate of electron capture at the BC site.

Process (7):  $\text{Mu}_{\text{BC}}^+ + e_c^- \xrightarrow{\nu_{ac}} \text{Mu}_T^0$ :  $\nu_{ac} = n_e v_e \kappa_{\text{BC}}^{+/0}$   $\times \exp[-E_{\text{BC}/T}^{+/0}/kT]$  is the activated capture rate.

The transition from  $\text{Mu}_{\text{BC}}^0$  to  $\text{Mu}_T^0$  can be ignored because the reaction rate is much slower than  $\nu_i$ . Also, the transition from  $\text{Mu}_T^0$  to  $\text{Mu}_{\text{BC}}^+$  can be ignored since its rate is much smaller than  $\nu_a$ . Simple electron capture at the BC site [process (6)] followed by ionization [process (3)] was found to be an inefficient depolarization mechanism that could not reproduce the sharp drop in the rf asymmetry observed at high temperature. This results from the fast ionization rate and small hyperfine parameter of  $\text{Mu}_{\text{BC}}^0$ . To fit this drop it was necessary to include  $\text{Mu}_T^0$  in the charge-exchange cycle and to introduce the activated-capture transition [process (7)]. While process (6) was ignored for the  $p$ -type samples it is needed to model  $n$ -type data because of the high electron density and fast capture rate. Finally, hole capture by  $\text{Mu}_{\text{BC}}^0$  [process (4)] had to be included to describe the feature at 50 K in  $p$ -type samples. This was achieved in the model by adding the hole capture rate to the ionization rate  $\nu_i$ .

Process (4):  $\text{Mu}_{\text{BC}}^0 + h^+ \xrightarrow{\nu_h} \text{Mu}_{\text{BC}}^+$ :  $\nu_h = n_h v_h \sigma_{\text{BC}}^{0/+}$  is the hole capture rate at the BC site.

As shown above and discussed in Sec. VI, very simple temperature-dependent expressions are used for the various transition rates.  $\rho$ ,  $E$ ,  $\sigma$ , and  $\kappa$  are the vibrational prefactor, energy, capture cross section, and composite site-change–electron-capture cross section for the appropriate transition, and  $n_e$  and  $v_e$  ( $n_h$  and  $v_h$ ) are the carrier density and mean thermal velocity for electrons (holes).

The following integral rate equations describe the time evolution of polarization for the three states.  $P_0^{\text{Mu}_{\text{BC}}^+}$ ,  $P_0^{\text{Mu}_{\text{BC}}^0}$ , and  $P_0^{\text{Mu}_T^0}$  are the polarization at low temperature ( $T=0$ ) in each of the prompt states:

$$\begin{aligned} P^{\text{Mu}_{\text{BC}}^+}(t) = & P_0^{\text{Mu}_{\text{BC}}^+} G^{\text{Mu}_{\text{BC}}^+}(t) e^{-(\nu_c + \nu_{ac})t} \\ & + \nu_i \int_0^t P^{\text{Mu}_{\text{BC}}^0}(\tau) G^{\text{Mu}_{\text{BC}}^+}(t-\tau) \\ & \times e^{-(\nu_c + \nu_{ac})(t-\tau)} d\tau. \end{aligned} \quad (\text{A1})$$

$G^{\text{Mu}_{\text{BC}}^+}(t)$  is the time evolution of the polarization while in the  $\text{Mu}_{\text{BC}}^+$  state; it is equal to  $\cos\omega_1 t$  on resonance and unity far off resonance:

$$\begin{aligned}
P^{\text{Mu}_{\text{BC}}^0}(t) = & P_0^{\text{Mu}_{\text{BC}}^0} G^{\text{Mu}_{\text{BC}}^0}(t) e^{-\nu_i t} + \nu_c \int_0^t P^{\text{Mu}_{\text{BC}}^+}(\tau) G^{\text{Mu}_{\text{BC}}^0}(t-\tau) e^{-\nu_i(t-\tau)} d\tau \\
& + \nu_a \int_0^t P^{\text{Mu}_T^0}(\tau) G^{\text{Mu}_{\text{BC}}^0}(t-\tau) e^{-\nu_i(t-\tau)} d\tau.
\end{aligned} \tag{A2}$$

$G^{\text{Mu}_{\text{BC}}^0}(t)$  is obtained from the anisotropic  $\text{Mu}_{\text{BC}}^0$  spin dynamics discussed in Appendix B:

$$P^{\text{Mu}_T^0}(t) = P_0^{\text{Mu}_T^0} \alpha e^{-\nu_a t} + \nu_{ac} \alpha \int_0^t P^{\text{Mu}_{\text{BC}}^+}(\tau) e^{-\nu_a(t-\tau)} d\tau. \tag{A3}$$

The factor  $\alpha$  represents the fraction of the  $\text{Mu}_T^0$  polarization retained in the direction of the applied field due to the oscillation of the mixed state. If the lifetime of the  $\text{Mu}_T^0$  state is long compared to the period of the hyperfine oscillation (which is true in our case) then  $\alpha = 1 - a_{24}$ , where  $a_{24}$  is the muonium precession amplitude for the 2–4 transition. In the high-field limit  $a_{24} \approx \frac{1}{2}(\omega_0/\omega_e)^2$ ;  $\omega_0$  is the  $\text{Mu}_T^0$  hyperfine frequency and  $\omega_e$  is the precession frequency of isolated electrons;<sup>2</sup>  $\alpha \approx 0.94$  at 2 kG.

Laplace transforms of the polarization are

$$\begin{aligned}
\bar{P}^{\text{Mu}_{\text{BC}}^+}(s) = & \frac{P_0^{\text{Mu}_{\text{BC}}^+} + \left[ P_0^{\text{Mu}_{\text{BC}}^0} + P_0^{\text{Mu}_T^0} \frac{\nu_a \alpha}{s + \nu_a} \right] \nu_i \bar{G}^{\text{Mu}_{\text{BC}}^0}(s + \nu_i)}{1 - \left[ \nu_c + \frac{\nu_a \nu_{ac} \alpha}{s + \nu_a} \right] \nu_i \bar{G}^{\text{Mu}_{\text{BC}}^+}(s + \nu_c + \nu_{ac}) \bar{G}^{\text{Mu}_{\text{BC}}^0}(s + \nu_i)} \bar{G}^{\text{Mu}_{\text{BC}}^+}(s + \nu_c + \nu_{ac}),
\end{aligned} \tag{A4}$$

$$\bar{P}^{\text{Mu}_T^0}(s) = \left[ P_0^{\text{Mu}_T^0} + \bar{P}^{\text{Mu}_{\text{BC}}^+}(s) \nu_{ac} \right] \frac{\alpha}{s + \nu_a}, \tag{A5}$$

$$\bar{P}^{\text{Mu}_{\text{BC}}^0}(s) = \left[ P_0^{\text{Mu}_{\text{BC}}^0} + \bar{P}^{\text{Mu}_{\text{BC}}^+}(s) \nu_c + \bar{P}^{\text{Mu}_T^0}(s) \nu_a \right] \bar{G}^{\text{Mu}_{\text{BC}}^0}(s + \nu_i). \tag{A6}$$

Equation (A4) is then substituted into Eq. (6.1) and evaluated with  $s = \nu_\mu$  to fit the rf asymmetry for the diamagnetic signal.

Processes involving the  $\text{Mu}_T^-$  state are discussed in Sec. II and Fig. 1(c). Two processes lead to the formation of  $\text{Mu}_T^-$ .

Process (2):  $\text{Mu}_T^0 + e_c^- \xrightarrow{\nu_c^-} \text{Mu}_T^-$ :  $\nu_c^- = n_e \nu_e \sigma_T^{0/-}$  is the rate of electron capture by  $\text{Mu}_T^0$  to form  $\text{Mu}_T^-$ .

Process (5):  $\text{Mu}_{\text{BC}}^0 + e_c^- \xrightarrow{\nu_{ac}^-} \text{Mu}_T^-$ :  $\nu_{ac}^- = n_e \nu_e \kappa_{\text{BC}/T}^{0/-} \exp[-E_{\text{BC}/T}^{0/-}/kT]$  is the activated capture rate.

$\text{Mu}_T^-$  is present in  $n$ -type samples at low temperature. Since under the present experimental conditions the two charge states behave identically one can replace the  $\text{Mu}_{\text{BC}}^+$  state by  $\text{Mu}_{\text{BC}}^+/\text{Mu}_T^-$  [Fig. 1(c)]. By modifying the above equations to include the transition from  $\text{Mu}_T^0$  to  $\text{Mu}_{\text{BC}}^+/\text{Mu}_T^-$ , process (2), and replacing the transition rate for process (3) by the rate for process (5), and since the charge state is negative setting  $\nu_c$  to 0, it is possible to fit and model the data for the  $n$ -type samples at low temperature.

Finally, the states and transitions used to describe the  $p$ -type data apply at high temperature to the  $n$ -type material up to  $N14$ . At elevated temperature the  $\text{Mu}_T^-$  state does not form because the rate leading to  $\text{Mu}_{\text{BC}}^+$  becomes faster than the transition rate to  $\text{Mu}_T^-$ . The temperature at which the change from mainly  $\text{Mu}_T^-$  to mostly  $\text{Mu}_{\text{BC}}^+$  takes place depends on the dopant concentration, with maximum overlap of the two charged

states occurring for intermediate electron densities. This treatment of the  $n$ -type data with a modified three-state model works well for the heavily doped samples like  $N15$  below room temperature from which most of the dynamic parameters relating to the  $\text{Mu}_T^-$  charge state were obtained. An important question remains concerning the role of thermal loss of an electron from  $\text{Mu}_T^-$ , process (8), in controlling the shift to higher temperatures for the drop in diamagnetic signal amplitude for highly doped  $n$ -type samples. Resolution of this question depends on the development of a more complete four-state model that will describe muonium dynamics in the  $n$ -type material.

## APPENDIX B: EFFECTIVE-FIELD CALCULATION

A dynamic calculation for the muon spin polarization using either the three- or four-state model requires evaluation of the spin dynamics in a highly anisotropic paramagnetic state. Specifically these models need the polarization transferred in the transition  $\text{Mu}_{\text{BC}}^0 \rightarrow \text{Mu}_{\text{BC}}^+$  which occurs around 120–160 K. Also, as implantation at low temperatures equally populates each of the available  $\langle 111 \rangle$   $\text{Mu}_{\text{BC}}^0$  sites, an appropriately weighted sum of these must be properly folded into the theory for an arbitrary field direction.

Such a calculation is greatly simplified when the external field strength is such that the electron Zeeman interaction dominates all other terms in the spin Hamiltonian. In these circumstances, the evolution of the

muon spin polarization is a sum of three processes, two of which dominate. Specifically, about half the polarization precesses in an effective field generated by the up electrons, half precesses in a second effective field imposed by the down electrons, and a third very small component oscillates at the electronic Larmor frequency. Because essentially all of the polarization is accounted for by the precession in these effective fields, it is sufficient to deal only with the first two components. A detailed derivation of all the terms is given in Ref. 25, with a preliminary discussion in Ref. 26.

In the absence of a transition, the prompt  $\text{Mu}_{\text{BC}}^0$  at a site along one of the four structurally equivalent  $\langle 111 \rangle$  axes defines, with respect to the external field, an angle and an occupation fraction  $\theta_j$  and  $f_j$ , respectively. For each  $\theta_j$  the detected muon polarization will consist of terms resulting from the two distinct precession patterns, caused by the effective field from the up (i.e., parallel to the external field) and down muonium electrons. The strength of these effective fields in units of  $\gamma_\mu$  are  $\omega_\mu^{\uparrow j}$  and  $\omega_\mu^{\downarrow j}$ , and are directed along polar angles  $\vartheta_\mu^{\uparrow j}(\theta_j)$  and

$\vartheta_\mu^{\downarrow j}(\theta_j)$  with respect to the  $\hat{z}$  axis.

The  $\hat{z}$  component of the polarization is detected in the rf  $\mu\text{SR}$  experiment, and the initial polarization is also along  $\hat{z}$ . For a given effective-field orientation the muon's polarization for a prompt  $\text{Mu}_{\text{BC}}^0$  state is then given by

$$P_z^{\text{Mu}_{\text{BC}}^0}(t) = \sum_j f_j [(\cos^2 \vartheta_\mu^{\uparrow j} + \sin^2 \vartheta_\mu^{\uparrow j} \cos \omega_\mu^{\uparrow j} t) + (\cos^2 \vartheta_\mu^{\downarrow j} + \sin^2 \vartheta_\mu^{\downarrow j} \cos \omega_\mu^{\downarrow j} t)] . \quad (\text{B1})$$

Examining the reaction  $\text{Mu}_{\text{BC}}^0 \xrightarrow{\nu_i} \text{Mu}_{\text{BC}}^0$  results in the following  $\text{Mu}^+$  polarization:

$$P_z^{\text{Mu}^+}(t) = \nu_i \int_0^t e^{-\nu_i \tau} P_z^{\text{Mu}^0}(\tau) d\tau , \quad (\text{B2})$$

where the BC subscript is implicitly understood. Utilizing (B1) and taking the normalized Laplace transform evaluated at  $s = \nu_\mu$  gives the polarization that an integral rf experiment would detect for the ionized final state. It is

$$P_z^{\text{Mu}^+}(s) = \nu_i \sum_j f_j \left[ \frac{\cos^2 \vartheta_\mu^{\uparrow j}}{s + \nu_i} + \frac{(s + \nu_i) \sin^2 \vartheta_\mu^{\uparrow j}}{(s + \nu_i)^2 + (\omega_\mu^{\uparrow j})^2} \right] + \left[ \frac{\cos^2 \vartheta_\mu^{\downarrow j}}{s + \nu_i} + \frac{(s + \nu_i) \sin^2 \vartheta_\mu^{\downarrow j}}{(s + \nu_i)^2 + (\omega_\mu^{\downarrow j})^2} \right] \Big|_{s=\nu_\mu} . \quad (\text{B3})$$

To complete the calculation the parameters which determine the effective fields must be established. The Hamiltonian governing the  $\text{Mu}_{\text{BC}}^0$  state is

$$\mathcal{H}_{\text{Mu}} = \gamma_e \mathcal{S}_z^e B - \gamma_\mu \mathcal{S}_z^\mu B - \gamma_n \mathcal{S}_z^n B + A_\mu \mathbf{S}_e \cdot \mathbf{S}_\mu + A_n \mathbf{S}_e \cdot \mathbf{S}_n + (D_\mu \mathbf{S}_\mu + D_n \mathbf{S}_n) \cdot (\hat{\mathbf{1}} - 3\hat{\mathbf{r}}\hat{\mathbf{r}}) \cdot \mathbf{S}_e . \quad (\text{B4})$$

The first three terms in (B4) are the Zeeman interactions in an external field  $\mathbf{B} = B\hat{z}$  with gyromagnetic ratios  $\gamma$ . Next are the isotropic electron-muon and electron-nuclear hyperfine coupling terms and finally the muon and nuclear anisotropic hyperfine terms with dipolar symmetry and strength  $D_\mu$  and  $D_n$ , respectively, sharing a common symmetry axis  $\hat{\mathbf{r}}(\theta, \phi)$ . References 25 and 26 show that the effective Hamiltonian can be written approximately as

$$\begin{aligned} \mathcal{H}_{\text{Mu}}^{\text{eff}} = & |\uparrow\rangle\langle\uparrow| \left\{ \langle\uparrow|\mathcal{H}_{\text{Mu}}|\uparrow\rangle + \frac{\langle\uparrow|\mathcal{H}_{\text{Mu}}|\downarrow\rangle\langle\downarrow|\mathcal{H}_{\text{Mu}}|\uparrow\rangle}{\omega_e} \right\} + |\downarrow\rangle\langle\downarrow| \left\{ \langle\downarrow|\mathcal{H}_{\text{Mu}}|\downarrow\rangle - \frac{\langle\downarrow|\mathcal{H}_{\text{Mu}}|\uparrow\rangle\langle\uparrow|\mathcal{H}_{\text{Mu}}|\downarrow\rangle}{\omega_e} \right\} \\ = & |\uparrow\rangle\langle\uparrow|\mathcal{H}_{\text{Mu}}^\uparrow + |\downarrow\rangle\langle\downarrow|\mathcal{H}_{\text{Mu}}^\downarrow . \end{aligned} \quad (\text{B5})$$

Applying this transformation to  $\mathcal{H}_{\text{Mu}}$  yields a set of terms in the up and down manifolds which contain single-particle interactions for muon and nuclei as well as bilinear interactions (responsible for any level-crossing effects). Specifically we have

$$\mathcal{H}_{\text{Mu}}^\uparrow = \frac{1}{2}\omega_e + \omega_\mu^\uparrow \cdot \mathbf{S}_\mu + \sum_n \omega_n^\uparrow \cdot \mathbf{S}_n + \mathcal{H}_j^\uparrow + \sum_\zeta \text{const} \times [O(1/\omega_e), \theta, \zeta] , \quad (\text{B6})$$

$$\mathcal{H}_{\text{Mu}}^\downarrow = -\frac{1}{2}\omega_e + \omega_\mu^\downarrow \cdot \mathbf{S}_\mu + \sum_n \omega_n^\downarrow \cdot \mathbf{S}_n + \mathcal{H}_j^\downarrow - \sum_\zeta \text{const} \times [O(1/\omega_e), \theta, \zeta] , \quad (\text{B7})$$

which results in a set of muon effective fields

$$\begin{aligned} \omega_\mu^\uparrow = & \hat{z} \left[ -\omega_\mu + \left[ \frac{1}{2} - \frac{A_\mu}{4\omega_e} \right] A_\mu + \left[ \frac{1}{2} + \frac{A_\mu}{4\omega_e} \right] D_\mu (1 - 3 \cos^2 \theta) + \frac{D_\mu^2}{4\omega_e} (3 \sin^2 \theta - 1) \right] \\ & - \hat{\rho}(\phi) \frac{3}{2} D_\mu \left[ 1 + \frac{A_\mu + D_\mu}{2\omega_e} \right] \cos \theta \sin \theta , \end{aligned} \quad (\text{B8})$$

$$\begin{aligned} \omega_\mu^\downarrow = & \hat{z} \left[ -\omega_\mu - \left[ \frac{1}{2} + \frac{A_\mu}{4\omega_e} \right] A_\mu - \left[ \frac{1}{2} - \frac{A_\mu}{4\omega_e} \right] D_\mu (1 - 3 \cos^2 \theta) + \frac{D_\mu^2}{4\omega_e} (3 \sin^2 \theta - 1) \right] \\ & + \hat{\rho}(\phi) \frac{3}{2} D_\mu \left[ 1 - \frac{A_\mu + D_\mu}{2\omega_e} \right] \cos \theta \sin \theta , \end{aligned} \quad (\text{B9})$$

a similar set of nuclear effective fields, and a set of muon-nuclear effective interactions. These latter two sets having nuclear spin degrees of freedom can be ignored for the present circumstances since Si has only a small fraction of nonzero isotopes. The constant is the same for both the up and down manifolds; it is

$$\text{const} \times [O(1/\omega_e), \theta, \mu] = \frac{1}{8\omega_e} [A_\mu^2 + A_\mu D_\mu (3 \cos^2 \theta - 1) + D_\mu^2 (1 + \frac{3}{2} \sin^2 \theta)]. \quad (\text{B10})$$

This form of the Hamiltonian has decomposed the  $\text{Mu}_{\text{BC}}^0$  Hamiltonian into pieces similar to the common Zeeman and dipolar interactions found in magnetic resonance. For our case  $A_\mu/D_\mu = 67.33/25.257$  and for an external field of 0.2 T (where all the  $\text{Mu}^+$  experimental work was carried out) the strength  $|\omega_\mu|$  (in MHz) and the polar angle  $\vartheta_\mu$  (in degrees) of the effective fields are given in the following table:

$\hat{z}$	$\theta_j$	$f_j$	$ \omega_\mu^{\uparrow j} $	$\vartheta_\mu^{\uparrow j}$	$ \omega_\mu^{\downarrow j} $	$\vartheta_\mu^{\downarrow j}$
[1,1,1]	0	0.25	18.7,	0	35.5,	0
	70.53	0.75	19.1,	38.5	70.2,	9.8
[1,1,0]	35.26	0.5	18.9,	71.2	51.3,	20.4
	90	0.5	19.2,	0	73.4,	0
[1,0,0]	54.74	1	19.0,	69.8	63.3,	16.4

For the more general case, in order to justify the treatment of (B1), which is based solely on the muon's single-particle effective fields, there must be no effective muon-nuclear coupling or Hartmann-Hahn degeneracies, viz.  $|\omega_\mu - \omega_n| \leq \sqrt{\text{Tr}\{\mathcal{H}_j^2\}}$ , which might drive a muon-nuclear level crossing. Level-crossing studies in Ref. 8 have shown that these are indeed far removed from the field region of interest here.

With the use of the above table, coupled with (B1) we can now evaluate the effects of the charge-state transformation on the observed polarization in the rf- $\mu$ SR experiment. Recall that contrary to time-differential LF  $\mu$ SR this resonant technique detects the muon's LF polarization only after it has made the charge-state transition into the  $\text{Mu}^+$  state. Equation (B1) is composed of time-independent fractions and oscillating components. The

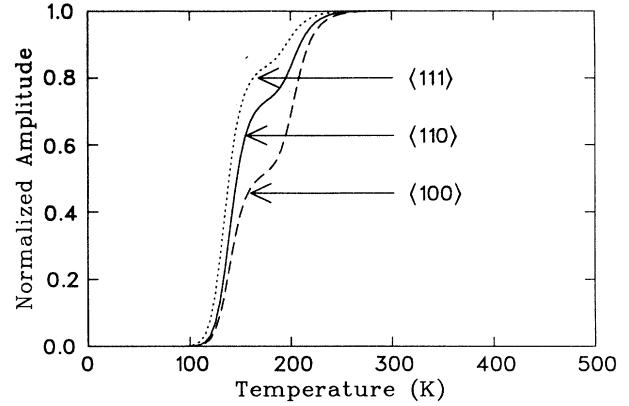


FIG. 9. The temperature and sample orientation dependence of the  $\text{Mu}_{\text{BC}}^+$  polarization detected in a rf experiment when a  $\text{Mu}_{\text{BC}}^0$  precursor state ionizes [process (3)].

time-independent part of the  $\text{Mu}_{\text{BC}}^0 \hat{z}$  polarization will be transferred intact when the transition rate surpasses the inverse muon lifetime. However, the oscillating parts will only survive a stochastic transition if the rate  $\nu_i$  becomes greater than the effective-field frequencies  $\omega_\mu^{\uparrow, \downarrow j}$ . For an activated rate  $\nu_i$  the various oscillating components of the  $\text{Mu}^0$  polarization will show up in the  $\text{Mu}^+$  polarization with different temperature dependencies.

The table indicates that for the  $\uparrow$  states all of the frequencies are about the same, since 0.2 T is very close to the magic field for  $\text{Mu}_{\text{BC}}^0$ . This means one can expect a sudden increase in the  $\text{Mu}^+$  amplitude to occur at a well-defined temperature for this fraction of the polarization. For the  $\downarrow$  states the effective fields are essentially lined up along the  $\hat{z}$  axis (i.e., the  $\vartheta_\mu^{\downarrow}$  are small), and the majority of the polarization is static and along the  $\hat{z}$  direction in any case. They contribute their polarization when the transition rate exceeds  $\nu_\mu$ .

For the temperature-dependent transition rate  $\nu_i$  used in the body of the paper, Fig. 9 shows the signature of what the RF experiment's detected  $\text{Mu}^+$  polarization would be like in the absence of any back reactions to the  $\text{Mu}_{\text{BC}}^0$  state.

<sup>1</sup>An overview of recent experimental and theoretical studies of hydrogen interaction with defects in crystalline solids is given by S. M. Myers, M. I. Baskes, H. K. Birnbaum, J. W. Corbett, G. G. DeLeo, S. K. Estreicher, E. E. Haller, P. Jena, N. M. Johnson, R. Kirchheim, S. J. Pearton, and M. J. Stavola, *Rev. Mod. Phys.* **64**, 559 (1992).

<sup>2</sup>A comprehensive review of muon studies in semiconductors up to 1988 is given by B. D. Patterson, *Rev. Mod. Phys.* **60**, 69 (1988).

<sup>3</sup>A summary of the recent muon results in semiconductors is

given by R. F. Kiefl and T. L. Estle, in *Hydrogen in Semiconductors*, edited by J. Pankove and N. M. Johnson (Academic, New York, 1990), p. 547.

<sup>4</sup>K. H. Chow, R. F. Kiefl, J. W. Schneider, B. Hitti, T. L. Estle, R. L. Lichti, C. Schwab, R. C. DuVarney, S. R. Kreitzman, W. A. MacFarlane, and M. Senba, *Phys. Rev. B* **47**, 16004 (1993).

<sup>5</sup>A review of rf resonance techniques for continuous muon beams is given by S. R. Kreitzman, *Hyperfine Interact.* **65**, 1055 (1990).

- <sup>6</sup>B. Hitti, S. R. Kreitzman, T. L. Estle, R. L. Lichti, K. H. Chow, J. W. Schneider, C. D. Lamp, and P. Mendels, *Hyperfine Interact.* **86**, 673 (1994).
- <sup>7</sup>R. L. Lichti, K. H. Chow, T. L. Estle, B. Hitti, R. F. Kiefl, S. R. Kreitzman, and J. W. Schneider, *Mater. Sci. Forum* **143-147**, 915 (1994).
- <sup>8</sup>R. F. Kiefl, M. Celio, T. L. Estle, S. R. Kreitzman, G. M. Luke, T. M. Riseman, and E. J. Ansaldo, *Phys. Rev. Lett.* **60**, 224 (1988).
- <sup>9</sup>S. F. J. Cox and M. C. R. Symons, *Chem. Phys. Lett.* **126**, 516 (1986).
- <sup>10</sup>T. L. Estle, S. K. Estreicher, and D. S. Marynick, *Hyperfine Interact.* **32**, 637 (1986); *Phys. Rev. Lett.* **58**, 1547 (1987); S. K. Estreicher, *Phys. Rev. B* **32**, 9122 (1987).
- <sup>11</sup>Yu. V. Gorelkinskii and N. N. Nevinnyi, *Pis'ma Zh. Tekh. Fiz.* **13**, 105 (1987) [*Sov. Tech. Phys. Lett.* **13**, 45 (1987)].
- <sup>12</sup>K. J. Chang and D. J. Chadi, *Phys. Rev. Lett.* **60**, 1422 (1988); C. G. Van de Walle, Y. Bar-Yam, and S. T. Pantelides, *ibid.* **60**, 2761 (1988).
- <sup>13</sup>N. M. Johnson, C. Herring, and C. G. Van de Walle, *Phys. Rev. Lett.* **73**, 130 (1994).
- <sup>14</sup>K. H. Chow, R. F. Kiefl, J. W. Schneider, T. L. Estle, B. Hitti, R. L. Lichti, C. Schwab, S. R. Kreitzman, R. C. DuVarney, M. Senba, J. Sonier, T. M. S. Johnston, and W. A. MacFarlane, *Hyperfine Interact.* **86**, 693 (1994).
- <sup>15</sup>S. K. Estreicher, M. A. Roberson, and Dj. M. Maric, *Phys. Rev. B* **50**, 17018 (1994).
- <sup>16</sup>H. Simmler, P. Eschle, H. Keller, W. Kündig, W. Odermatt, B. D. Patterson, B. Pümpin, I. M. Savić, J. W. Schneider, U. Straumann, and P. Truöl. *Hyperfine Interact.* **64**, 535 (1990); *Mater. Sci. Forum* **83-87**, 1121 (1992).
- <sup>17</sup>J. H. Brewer and K. M. Crowe, *Annu. Rev. Nucl. Part. Sci.* **28**, 239 (1978).
- <sup>18</sup>I. J. Lowe and M. Engelsberg, *Rev. Sci. Instrum.* **45**, 631 (1974).
- <sup>19</sup>I. J. Lowe and D. W. Whitson, *Rev. Sci. Instrum.* **48**, 268 (1977).
- <sup>20</sup>K. H. Chow, R. L. Lichti, R. F. Kiefl, S. Dunsiger, T. L. Estle, B. Hitti, R. Kadono, W. A. MacFarlane, J. W. Schneider, D. Schumann, and M. Shelley, *Phys. Rev. B* **50**, 8918 (1994).
- <sup>21</sup>S. R. Kreitzman, T. L. Estle, B. Hitti, J. W. Schneider, K. H. Chow, and R. L. Lichti, *Hyperfine Interact.* **87**, 1063 (1994).
- <sup>22</sup>B. Holm, K. Bonde-Nielsen, and B. Bech-Nielsen, *Phys. Rev. Lett.* **66**, 2360 (1991).
- <sup>23</sup>B. Bech-Nielsen, K. Bonde-Nielsen, and J. R. Byberg, *Mater. Sci. Forum* **143-147**, 909 (1994).
- <sup>24</sup>Yu. V. Gorelkinski and N. N. Nevinnyi, *Physica B* **170**, 155 (1992).
- <sup>25</sup>S. Kreitzman and E. Roduner, *Chem. Phys.* **192**, 189 (1995).
- <sup>26</sup>R. Kiefl and S. Kreitzman, in *Perspectives in Muon Science*, edited by T. Yamazaki, K. Nakai, and K. Nagamine (Elsevier, New York, 1992), p. 265.